

NAT'L INST OF STAND & TECH

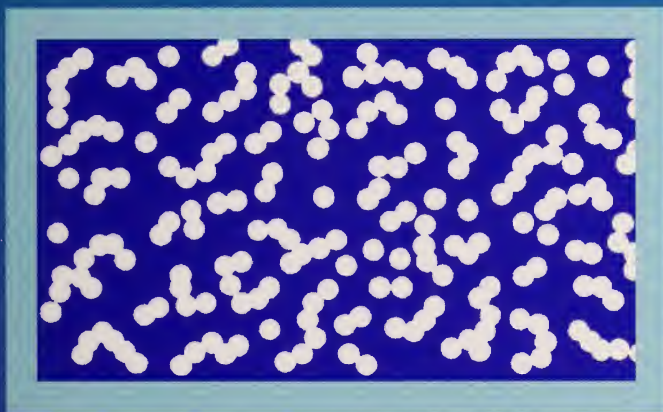


A11107 049631

NIST  
PUBLICATIONS

REFERENCE

# Pore Characterization in Low-k Dielectric Films Using X-ray Reflectivity: X-ray Porosimetry



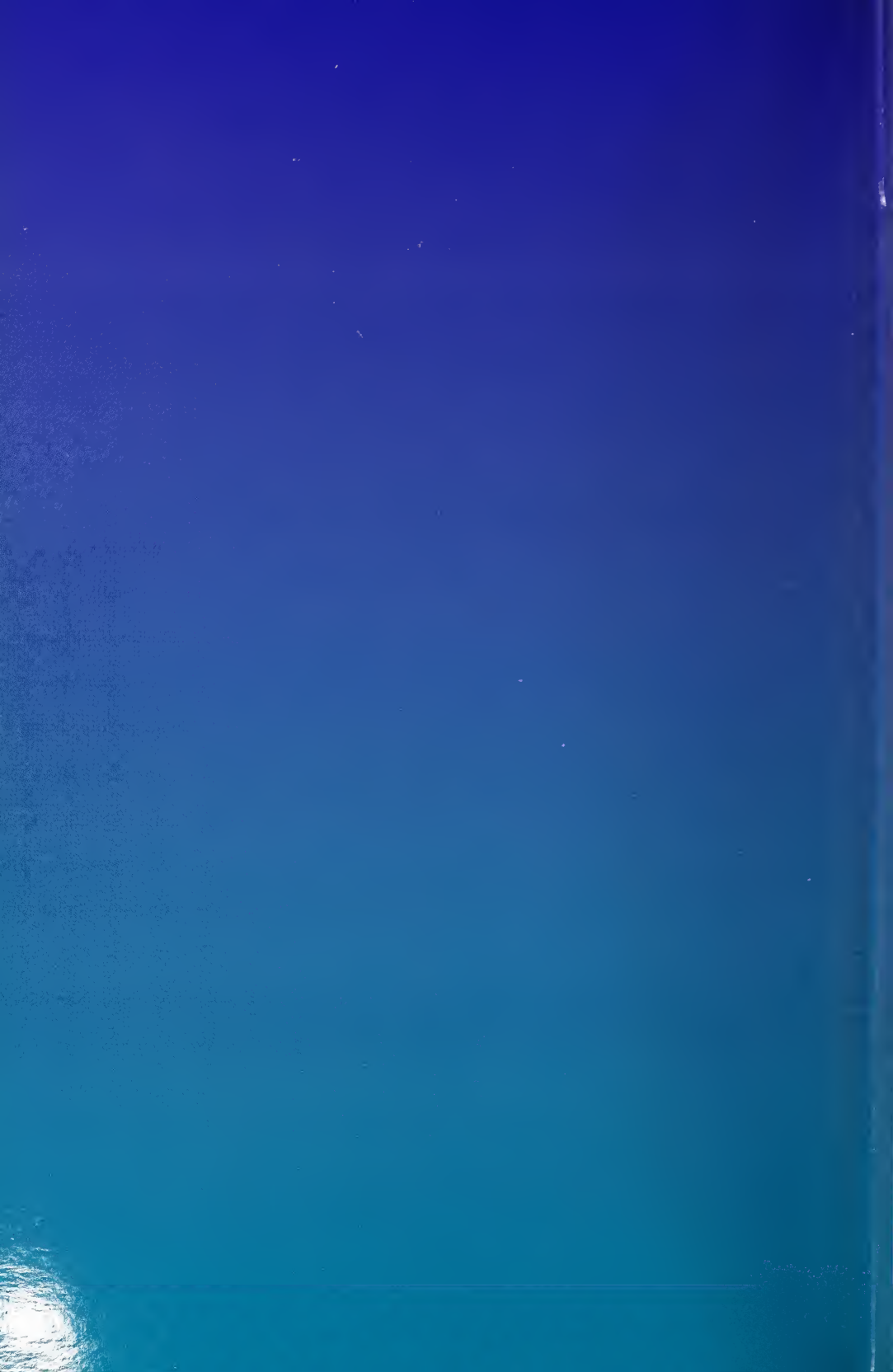
Christopher L. Soles, Hae-Jeong Lee,  
Eric K. Lin, and Wen-li Wu

NIST

National Institute of  
Standards and Technology  
Technology Administration  
U.S. Department of Commerce

Special  
Publication  
960-13

QC  
100  
.U57  
#960-13  
2004



# NIST Recommended Practice Guide

Special Publication 960-13

## **Pore Characterization in Low-k Dielectric Films Using X-ray Reflectivity: X-ray Porosimetry**

Christopher L. Soles, Hae-Jeong Lee,  
Eric K. Lin, and Wen-li Wu

NIST Polymers Division

June 2004



**U.S. Department of Commerce**

Donald L. Evans, Secretary

**Technology Administration**

Phillip J. Bond, Undersecretary for Technology

**National Institute of Standards and Technology**

Arden L. Bement, Jr., Director

Certain commercial entities, equipment, or materials may be identified in this document in order to describe an experimental procedure or concept adequately. Such identification is not intended to imply recommendation or endorsement by the National Institute of Standards and Technology, nor is it intended to imply that the entities, materials, or equipment are necessarily the best available for the purpose.

---

National Institute of Standards and Technology  
Special Publication 960-13  
Natl. Inst. Stand. Technol.  
Spec. Publ. 960-13  
68 pages (June 2004)  
CODEN: NSPUE2

U.S. GOVERNMENT PRINTING OFFICE  
WASHINGTON: 2004

For sale by the Superintendent of Documents  
U.S. Government Printing Office  
Internet: [bookstore.gpo.gov](http://bookstore.gpo.gov) Phone: (202) 512-1800 Fax: (202) 512-2250  
Mail: Stop SSOP, Washington, DC 20402-0001

## FOREWORD

The persistent miniaturization or rescaling of the integrated chip (IC) has led to interconnect dimensions that continue to decrease in physical size. This, coupled with the drive for reduced IC operating voltages and decreased signal-to-noise ratio in the device circuitry, requires new interlayer dielectric (ILD) materials to construct smaller and more efficient devices. At the current 90 nm technology node, fully dense organosilicate materials provide sufficient ILD shielding within the interconnect junctions. However, for the ensuing 65 nm and 45 nm technology nodes, porous ILD materials are needed to further decrease the dielectric constant  $k$  of these critical insulating layers. The challenge to generate sufficient porosity in sub-100 nm features and films is a significant one. Increased levels of porosity are extremely effective at decreasing  $k$ , but high levels of porosity deteriorate the mechanical properties of the ILD structures. Mechanically robust ILD materials are needed to withstand the stresses and strains inherent to the chemical–mechanical polishing steps in IC fabrication. To optimize both  $k$  and the mechanical integrity of sub-100 nm ILD structures requires exacting control over the pore formation processes. The first step in achieving this goal is to develop highly sensitive metrologies that can accurately quantify the structural attributes of these nanoporous materials. This *Recommended Practice Guide* is dedicated to developing X-ray Porosimetry (XRP) as such a metrology. It is envisaged that XRP will facilitate the development of nanoporous ILD materials, help optimize processing and fabrication parameters, and serve as a valuable quality control metrology. Looking beyond CMOS technology, many attributes of XRP will be useful for the general characterization of nanoporous materials which are becoming increasingly important in many emerging fields of nanotechnology.



## ACKNOWLEDGMENTS

The authors would like to thank the many individuals who over the past several years directly contributed to our low- $k$  dielectrics characterization project. These individuals include Barry Bauer, Ronald Hedden, Da-Wei Liu, Bryan Vogt, William Wallace, Howard Wang, Michael Silverstein, Gary Lynn, Todd Ryan, Jeff Wetzel, and a long list of collaborators identified in reference [4]. In addition, we are also grateful for the support from the NIST Office of Microelectronics Programs and International SEMATECH. Without their financial backing, this work would not have been possible. Finally, a special debt of thanks goes to Barry Bauer and Ronald Hedden who were especially instrumental in completing this *Recommended Practice Guide*.







## TABLE OF CONTENTS

<i>List of Figures .....</i>	<i>ix</i>
<i>List of Tables .....</i>	<i>x</i>
<b>I. INTRODUCTION .....</b>	<b>1</b>
1.A. <i>Basics of Porosimetry .....</i>	<i>2</i>
1.B. <i>The Concept of X-ray Porosimetry .....</i>	<i>5</i>
1.C. <i>Fundamentals of Specular X-ray Reflectivity .....</i>	<i>5</i>
1.C.1. <i>Reflectivity from a Smooth Surface .....</i>	<i>7</i>
1.C.2. <i>Reflectivity from a Thin Film on a                 Smooth Substrate .....</i>	<i>9</i>
<b>II. EXPERIMENTAL .....</b>	<b>13</b>
2.A. <i>X-ray Reflectometer Requirements .....</i>	<i>13</i>
2.A.1. <i>Resolution Effects .....</i>	<i>17</i>
2.A.2. <i>Recommended Procedure for Sample                 Alignment.....</i>	<i>19</i>
2.B. <i>Methods of Partial Pressure Control .....</i>	<i>24</i>
2.B.1. <i>Isothermal Mixing with Carrier Gases .....</i>	<i>24</i>
2.B.2. <i>Sample Temperature Variations in a                 Vapor Saturated Carrier Gas.....</i>	<i>28</i>
2.B.3. <i>Pure Solvent Vapor .....</i>	<i>30</i>
2.B.4. <i>Choice of Adsorbate .....</i>	<i>31</i>
<b>III. DATA REDUCTION AND ANALYSIS .....</b>	<b>33</b>
3.A. <i>Reducing the X-ray Reflectivity Data .....</i>	<i>33</i>
3.B. <i>Fitting the X-ray Reflectivity Data .....</i>	<i>35</i>
3.C. <i>Interpretation of the XRP Data .....</i>	<i>35</i>

<b>3.D. Special Concerns .....</b>	<b>47</b>
<b>3.D.1. Quantitative Interpretation of the           Physisorption Isotherms .....</b>	<b>47</b>
<b>3.D.2. Isothermal Control .....</b>	<b>49</b>
<b>3.D.3. Time Dependence of Desorption .....</b>	<b>50</b>
<b>3.D.4. P versus T Variations of <math>P/P_0</math> .....</b>	<b>52</b>
 <b>IV. SUMMARY .....</b>	 <b>53</b>
 <b>V. REFERENCES .....</b>	 <b>55</b>

## List of Figures

Figure 1.	Schematic illustration of the six main types of gas physisorption isotherms, according to the IUPAC classification scheme. ....	3
Figure 2.	Calculated X-ray reflectivity results from silicon surface with different surface roughness. The solid and dashed curves correspond to RMS surface roughness values of 1 Å and 10 Å, respectively .....	8
Figure 3.	Calculated X-ray reflectivity data for Si surfaces with different linear absorption coefficients. The solid curve corresponds to a nominal absorption coefficient of $\mu = 1.47 \times 10^{-6} \text{ Å}^{-1}$ for pure Si, while the dashed curve indicates an order of magnitude increase, $\mu = 1.47 \times 10^{-5} \text{ Å}^{-1}$ .....	9
Figure 4.	Part (a) displays the low $Q$ theoretical X-ray reflectivity for a 3000 Å thick PS film supported on a Si wafer; the inset extends the reflectivity to high $Q$ . The marked decrease in the reflectivity at $Q = 0.022 \text{ Å}^{-1}$ and $0.032 \text{ Å}^{-1}$ corresponds to the $Q_c$ values of PS and Si, respectively. The region between these two $Q_c$ values is the wave-guiding region of the reflectivity curve. Part (b) illustrates how a ten-fold increase in the linear absorption coefficient $\mu$ of the film significantly affects the reflected intensities in this wave-guiding region .....	10
Figure 5.	The diagram in part (a) depicts the relevant degrees of freedom for an X-ray reflectometer. In this representation, $\theta$ defines goniometer angles for both the incident X-ray beam and the detector position (x-ray optics) while $\Omega$ , $\Phi$ , and $z$ are the tilt, yaw, and vertical translation ( $x$ and $y$ would be the lateral translations) of the sample stage. The X-ray goniometer and sample stage move/rotate on separate goniometers, $G_x$ and $G_s$ respectively, as shown in part (b), and it is advisable to make these circles concentric. It is critical that the X-ray beam passes through the center $O$ of the $G_x$ ; detector and X-ray source positions $D'$ and $S'$ where the beam does not pass through the origin are unacceptable, as discussed in the text .....	14
Figure 6.	Calculated X-ray reflectivity curves for a 1 μm PS film with instrumental angular divergences of ( $3 \times 10^{-5}$ , $6 \times 10^{-5}$ and $1.2 \times 10^{-4}$ ) rad in both the wave-guiding (part a) and high $Q$ (part b) regimes. Increasing angular divergence significantly damps the interference fringes, especially at low $Q$ within the wave-guiding regime .....	18

- Figure 7. Theoretical X-ray reflectivity curves for a 1  $\mu\text{m}$  PS film with two different wavelength dispersions. The solid line corresponds to a wavelength dispersion (wd) of  $\delta\lambda/\lambda = 6 \times 10^{-5}$  while the dotted line denotes  $\delta\lambda/\lambda = 6 \times 10^{-4}$ . The main body illustrates these effects in the low  $Q$  wave-guiding region while the inset emphasizes the high  $Q$  effects ..... 19
- Figure 8. Panels (a) through (e) illustrate the process required to align the X-ray reflectometer, as described in the text. In each panel, the dotted vertical line indicates the current zero position for each degree of freedom while the dashed line indicates the new position that should be reinitialized to zero. Data are presented for illustrating the alignment procedure only, so the standard uncertainties are irrelevant and not provided ..... 20
- Figure 9. A  $\theta$  scan of a well-aligned reflectometer. The pronounced peak (off the vertical scale of the plot) from the main beam defines the  $\theta = 0^\circ$  condition. The linear increase in intensity with the angle beyond the main beam peak comes from increasing the fraction of the beam that is focused onto the sample (footprint effect). Standard uncertainty in the intensity is less than the line width ..... 23
- Figure 10. Schematics depicting the different methods by which the partial pressure in the XRP sample chamber can be controlled. Part (a) is based on bubbling a carrier gas through a solvent reservoir while part (b) illustrates controlled flow of pure vapor into a chamber that is continually being evacuated by a vacuum pump ..... 25
- Figure 11. UV absorption spectra of mixtures of pure and toluene-saturated air with a total flow rate of 100 sccm. Starting with the flat featureless spectra showing nearly 0 absorbance (pure airflow), each successive curve indicates a 10 sccm increment in the flow rate of the toluene-saturated air and a 10 sccm decrement in the pure airflow rate. The ratio of the integrated areas between the curve of interest and the toluene-saturated curve, using the pure air curve as a baseline, defines  $P/P_0$ . The inset shows a linear correlation between the desired set-point and the measured  $P/P_0$ , with a least-squared deviation of  $\chi^2 = 0.0002$  ..... 26
- Figure 12. There are two ways in which  $r_c$  can be varied in the Kelvin equation.  $r_c$  values from approximately (1 to 250) Å can be obtained by mixing ratios of dry and toluene-saturated air at 20 °C. Likewise, a comparable range of pore sizes can be achieved by flowing air saturated in toluene at 20 °C across the sample and heating the film between 20 °C and 125 °C ..... 29

Figure 13. X-ray reflectivity data from a well-aligned sample and the intensity from the background as measured at an angle offset from the specular angle. The background level is indicated in the inset schematic. Standard uncertainties are smaller than the size of the data markers .....	34
Figure 14. SXR curves of porous HSQ, porous MSQ, and porous SiCOH thin films. The curves are offset for clarity. The standard uncertainty in $\log(I/I_0)$ is less than the line width .....	36
Figure 15. Critical angle changes for the porous HSQ sample as $P/P_0$ increases systematically from 0 (dry air) to 1 (toluene-saturated air). Condensation of the toluene inside the pores results in an appreciable and measurable change in $Q_c^2$ .....	39
Figure 16. Physisorption isotherms for the porous HSQ, MSQ, and SiCOH films. The lines are smooth fits using the cumulative sum of a sigmoidal and a log-normal function for porous HSQ and MSQ films, and the sum of a Gaussian and a sigmoidal function for porous SiCOH film. We generally recommend fitting these physisorption isotherms with such arbitrary fit functions. If the curve faithfully parameterizes the experimental data, it will be helpful later in extracting a smooth pore size distribution (discussed later in Figure 18). Estimated standard uncertainties are comparable to the size of the data markers .....	40
Figure 17. Schematic pore structures for the porous HSQ, MSQ, and SiCOH films .....	41
Figure 18. Approximate pore size distributions from the fits (not data) through the physisorption isotherms in Figure 16, using Eq. (1) used to convert $P/P_0$ into a pore size. The distributions from the adsorption branch (solid lines) can be significantly broader and shifted to larger pore sizes than the corresponding desorption branch, especially in those materials (like the MSQ film) with a large distribution of mesopore sizes .....	42
Figure 19. SANS data for the porous HSQ (circles), MSQ (diamonds), and SiCOH (triangles) films under vacuum. Error bars, usually small than the data markers, indicate the standard uncertainty in the absolute intensity .....	44



- Figure 20. XRP data for a low- $k$  film comprised of 3 distinct layers. Part (a) shows the reflectivity data for the dry and toluene-saturated films, revealing both a high-frequency periodicity due to the total film thickness and low-frequency oscillations due to the thinner individual layers. Part (b) shows the real space scattering length density profiles as a function of distance into the film, revealing the thickness and density of the individual layers ..... 46
- Figure 21. Physisorption isotherms generated by the  $T$  (squares) and  $P$  (all other data markers) variation methodologies of controlling  $P/P_0$ , as described in the text. The two techniques do not produce isotherms indicating that adsorption is not temperature invariant. Notice the discontinuous nature of the desorption pathways of the  $P$  variation technique. These discontinuities can be attributed to insufficient equilibration times, as described in the text and in reference to Figure 22. The estimated standard uncertainty in  $Q_c^2$  is comparable to the size of the data markers ..... 50
- Figure 22. Time dependence of the  $Q_c^2$  variations in the porous HSQ sample after  $P/P_0$  jumps from 1.0 to 0.36 (squares) and 1.0 to 0.28 (circles). Notice that  $Q_c^2$  continues to evolve for several hours after the jump, indicating the equilibrium is difficult to achieve on the desorption branch. The same time dependence is curiously absent upon adsorption. The estimated standard uncertainty in  $Q_c^2$  is comparable to the size of the data markers ..... 51

## List of Tables

Table 1:	A summary of the atomic compositions, dielectric constants ( $k$ ), and structural characteristics of different porous low- $k$ films. The estimated standard uncertainties of the atomic compositions, $Q_c^2$ , densities, porosities and pore radii are $\pm 2\%$ , $0.05 \text{ \AA}^{-2}$ , $0.05 \text{ g/cm}^3$ , $1\%$ , and $1 \text{ \AA}$ , respectively .....	39
----------	---	----





# 1. INTRODUCTION

Increased miniaturization of the integrated chip has largely been responsible for the rapid advances in semiconductor device performance, driving the industry's growth over the past decade(s). Soon the minimum feature size in a typical integrated circuit device will be well below 100 nm. At these dimensions, interlayers with extremely low dielectric constants ( $k$ ) are imperative to reduce the cross-talk between adjacent lines and also enhance device speed. State-of-the-art non-porous, silicon-based low- $k$  dielectric materials have  $k$  values on the order of 2.7. However,  $k$  needs to be further reduced to keep pace with the demand for increased miniaturization. There are a number of potential material systems for these next generation low- $k$  dielectrics, including organosilsesquioxane resins, sol-gel based silicate materials, chemical-vapor deposited silica, and polymeric resins. It is not yet evident as to which material(s) will ultimately prevail. Nevertheless, it has become apparent that decreasing  $k$  beyond current values universally requires generating significant levels of porosity within the film; sufficiently low enough dielectric constants are not feasible with fully dense materials.

The demand of increased porosity in reduced dimensions faces many challenges. To generate extensive porosity in sub-500 nm films and/or features requires exacting control of the pore generation process. The first step towards achieving this control, before addressing materials concerns, is developing metrologies that quantitatively characterize the physical pore structure with accuracy and reproducibility in terms of porosity, average pore size, pore size distribution, etc. Porosimetry, that is pore characterization from a measurable response to liquid intrusion into the porous material, is a mature field. There are several techniques, such as gas adsorption, mercury intrusion, mass uptake, etc., capable of characterizing pores significantly smaller than 100 nm. However, these traditional methods lack the sensitivity to quantify porosity in thin, low- $k$  films. The sample mass in a 500 nm thick film will be less than a few mg and the usual observables (*i.e.*, pressure in a gas adsorption experiment or mass in an gravimetric experiment) exhibit exceedingly small changes as the pores are filled with the condensate. Thin film porosimetry requires extraordinary sensitivity.

Currently, there are only a few techniques suitable for the on-wafer characterization of the pore structures in low- $k$  dielectric films. The most widely known include positronium annihilation lifetime spectroscopy (PALS),<sup>[1,2]</sup> ellipsometric porosimetry (EP),<sup>[3]</sup> and scattering-based techniques utilizing either neutrons or X-rays.<sup>[4]</sup> Each of these techniques comes with inherent strengths and weaknesses. PALS is well-suited for average pore size measurements when the pores are exceedingly small (*i.e.*, 2 nm to 20 nm

in diameter) and capable of quantifying closed pores not connected to the surface. However, PALS is also a high-vacuum technique (more difficult to implement) and non-trivial in terms of quantifying the total porosity. The neutron scattering measurements can be powerful but are severely limited by access to neutron scattering facilities. EP is very similar to the X-ray porosimetry technique described herein but critically relies upon the index of refraction for the sample and condensate being either known or approximated. This guide is dedicated to developing X-ray porosimetry as a powerful tool for characterizing porosity in thin, low-k dielectric films, both in terms of the requisite experimental set-up and the data interpretation. However, it is also important to realize that the utility of X-ray porosimetry extends beyond the semiconductor industry and the field of low-k dielectrics. The technique is generally applicable to porous media supported on a smooth, flat surface. Relevant or related applications include membranes, filters, catalyst supports, separation media, and other nanoporous materials.

### 1.A. Basics of Porosimetry

The field of porosimetry is a mature science with vast documentation in the literature. Traditional forms of porosimetry rely upon the surface adsorption and/or condensation of vapor inside the porous media. For example, it has been known for many years that charcoal (a naturally porous material) will adsorb large volumes of gas. The first quantitative measurements of this phenomenon appeared in the late 1700's [detailed in references 5, 6]. Over the next 200 or so years, the quantitative and scientific advances in these gaseous uptake measurements evolved into the modern-day field of porosimetry. To fully appreciate the current status of the porosimetry field, we recommend the following texts [7–9]. Today, the most common form of porosimetry is the nitrogen physisorption isotherm. In this method, the porous sample is sealed in a vessel of fixed volume, evacuated, and cooled to the boiling point liquid  $N_2$ . The sample vessel is then filled with a known quantity of pure  $N_2$  gas. The fixed volume of the vessel combined with the known volume of gas should define the partial pressure. However, at low-dosing pressures some of the  $N_2$  condenses on the surface of the sample, resulting in a reduction of the “predicted” pressure that can be measured with an accurate pressure transducer. From the pressure reduction and the volume, the amount of adsorbed  $N_2$  onto the pore surfaces can be calculated.

At higher pressures, after a few monolayers of the gas adsorb onto the pore walls,  $N_2$  begins to condense inside the smallest pores even though the vapor pressure in the system may be less than the liquid equilibrium vapor pressure. Zsigmondy<sup>[10]</sup> was the first to illustrate this effect and

described the process, using concepts originally proposed by Thompson (Lord Kelvin), as capillary condensation.<sup>[11]</sup> The classic Kelvin equation relates the critical radius for this capillary condensation,  $r_c$ , to the partial pressure  $P$ , equilibrium vapor pressure  $P_0$ , liquid surface tension  $\gamma$ , and molar volume  $V_m$  through:

$$r_c = \frac{2V_m\gamma}{-RT} \frac{1}{\ln(P/P_0)} \quad (1)$$

where  $T$  is the absolute temperature. This relation demonstrates that the critical (maximum) pore size for capillary condensation increases with the partial pressure, until the equilibrium vapor pressure of liquid  $N_2$  is achieved and  $r_c$  approaches infinity. In the porosimeter apparatus, capillary condensation leads to a noticeable pressure drop that directly yields the amount of adsorbed vapor. The volume of the adsorbed/condensed vapor is measured as the partial pressure first increases to saturation and then decreases back to zero. A plot of the volume of adsorbed condensate versus the partial pressure defines a physisorption isotherm. The International Union of Pure and Applied Chemistry (IUPAC) proposes that all physisorption isotherms are classified into six general types,<sup>[12]</sup> schematically depicted in Figure 1.

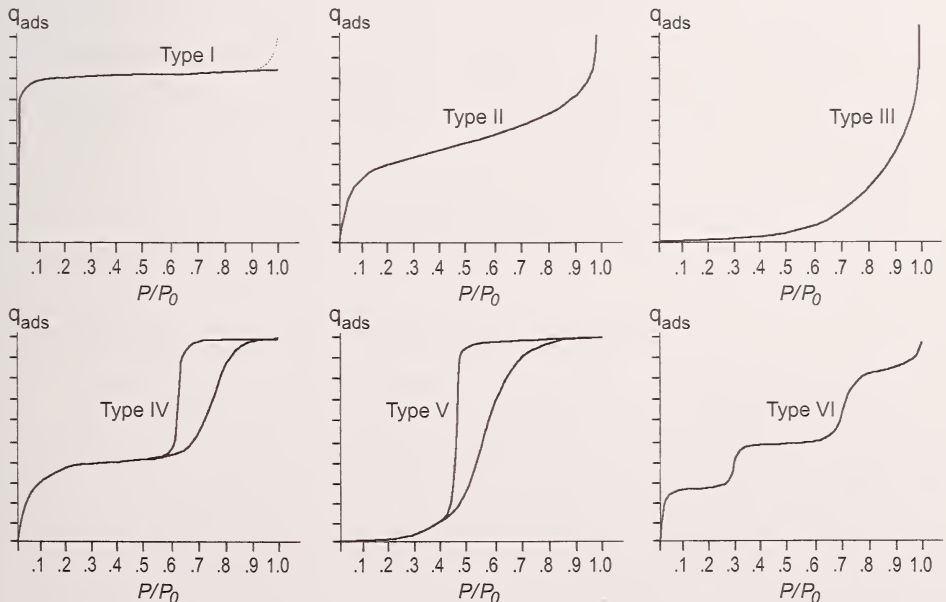


**Figure 1.** Schematic illustration of the six main types of gas physisorption isotherms, according to the IUPAC classification scheme.<sup>[12]</sup>

Before discussing these isotherms, we must establish the accepted pore size nomenclature. IUPAC classifies pores by their internal width,  $w$ , according to the following definitions<sup>[12,13]</sup>:

<i>micropores:</i>	$w < 20 \text{ \AA}$
<i>mesopores:</i>	$20 \text{ \AA} \leq w \leq 500 \text{ \AA}$
<i>macropores:</i>	$w > 500 \text{ \AA}$

A wealth of information about the pore structure can be obtained from the general isotherm classifications in Figure 1. For example, a strong increase at low partial pressures, like in Types I, II, IV, and VI, is usually indicative of enhanced or favorable adsorbent-adsorbate interactions as opposed to weak interactions in Type III or V. Initial uptakes that rapidly plateau, like Type I and the mid-stages of Type IV, are usually indicative of micropore filling, *i.e.*, pores that are comparable in dimension to the adsorbate molecule. The other possibility is that larger pores exist, and after an initial monolayer plateau, continued uptake occurs. This continued adsorption can be either gradual (Type II) or discrete in steps of additional monolayers (Type VI). There can also be hysteresis loops between the adsorption and desorption pathways at moderate partial pressures as seen in Type IV and V. Hysteresis loops are a signature of capillary condensation in mesopores. Finally, diverging uptakes near saturation, seen in Types II and III, are an indication of macropore filling. A more detailed description of these physisorption isotherms can be found in the general porosimetry literature.<sup>[7-9,12]</sup>

The preceding text discussed porosimetry in the context of  $N_2$  adsorption isotherms, with the amount of adsorbed gas determined from the pressure drop. One can also envisage monitoring other parameters to determine the uptake of adsorbate, such as the mass or heat of adsorption. However, these measurements become exceedingly difficult in thin films where there is limited sample mass. For example, a 500 nm thick, low- $k$  dielectric film might have an average density of  $1 \text{ g/cm}^3$  and a porosity of approximately 50 % by volume. This means that on a 7.62 cm (3") diameter wafer, there will be approximately  $1 \times 10^{-3} \text{ cm}^3$  of pore volume in comparison to the several grams of Si from the supporting substrate. Traditional porosimetry techniques lack the sensitivity to register the pressure, mass, or calorimetric changes that occur when condensing such a small amount of vapor; metrologies with higher sensitivity are critically needed to quantify the porosity in thin, low- $k$



dielectric films. It is also desirable that the characterization be *in-situ* on the supporting Si wafer. This circumvents sample damage and the inevitable errors (*i.e.*, the creation of rough surfaces, damage to existing pore structures, etc.) that result from scraping large quantities of low-k material off multiple wafers. *In-situ* techniques further retain the possibility of serving as on-line or process control checks in industrial fabrication settings. To this end, we have developed X-ray porosimetry as a viable and powerful tool for characterizing the pore structures of thin, low-k dielectric films.

## 1.B. The Concept of X-ray Porosimetry

In the following, we describe a form of porosimetry with the requisite sensitivity to quantify the small pore volumes in a thin, low-k dielectric film. The technique, known as X-ray porosimetry (which we abbreviate as XRP), combines specular X-ray reflectivity measurements with the mechanism capillary condensation. As will be described below, specular X-ray reflectivity is a means to characterize the density of thin films supported on a Si substrate. If the environment surrounding the film is gradually enriched with an organic vapor, like toluene, the vapor will condense in the pores with radii less than the critical radius for capillary condensation. This condensation increases the density of the sample appreciably. Recall earlier estimates that the density of a low-k film is on the order of  $1 \text{ g/cm}^3$  with approximately 50 % porosity (implying wall density on the order of  $2 \text{ g/cm}^3$ ). Given that most condensed organic vapors also have densities on the order of  $1 \text{ g/cm}^3$ , complete condensation leads to a significant (*i.e.*, on the order of 100 %) change in the total film density. This provides an effective means to monitor the vapor uptake as a function of partial pressure, mapping out physisorption isotherms similar to Figure 1. Before elaborating on the interpretation of these isotherms, we first need to review the relevant fundamentals of X-ray reflectivity.

## 1.C. Fundamentals of Specular X-ray Reflectivity

Specular X-ray reflectivity (SXR) is an established technique for measuring the thickness, density, and roughness of thin films.<sup>[14–18]</sup> For X-ray wavelengths of a few tenths of a nanometer, the refractive index of most materials is less than one. This implies that there is a critical angle,  $\theta_c$ , below which there is total external reflection of the incident X-ray radiation. In the typical SXR measurement, the reflected intensity is collected as the incident angle and detector position are scanned through equal angles  $\theta$  (the specular condition) from just below to well beyond  $\theta_c$ . The electron density profile perpendicular to the film surface can be

deduced by modeling the SXR data with a one-dimensional Schrödinger equation.<sup>[14, 19]</sup> Free-surface roughness, interfacial roughness between the layers, and density variations perpendicular through the film can be extracted from the reflectivity data by using computers to systematically vary model electron-density profiles to best fit the experimental data (see reference [19] for one such fitting algorithm). It is important to realize that the angles  $\theta$  can be quite shallow with respect to the surface parallel. This means that the footprint of the X-ray beam on the film is rather large, typically several  $\text{cm}^2$ ; data is collected from a large area of the sample. However, the coherence length of the X-ray beam (depending on the optics) is typically on the order of  $1\ \mu\text{m}$  or less, implying that the thickness, density, and roughness within the large footprint are sampled with only  $\mu\text{m}$  resolution. This is equivalent to using a  $1\ \mu\text{m}$  ruler to characterize a region of several  $\text{cm}^2$ ; locally the topology may appear flat, even if larger scale roughness exists. An example would be a film with visible, low-periodicity (period of say one mm) roughness but smooth surfaces on the  $\mu\text{m}$  length scale; SXR would perceive a smooth film with a thickness that was actually an average over all the low-frequency thickness variations.

At X-ray energies significantly higher than the absorption edges for any of the constituent elements in the sample, the electrons can be considered “free” in that anomalous X-ray scattering can be ignored. This assumption is valid for most laboratory based  $\text{Cu-K}_\alpha$  sources (used herein) because the typical elements encountered in the low- $k$  dielectric films are H, C, O, Si and possibly F. The refractive index,  $n$ , of a material with respect to the X-ray radiation is:

$$n = 1 - (\delta + i\beta) = 1 - \frac{r_0 \rho_e \lambda^2}{2\pi} - i \frac{\mu \lambda}{4\pi} \quad (2)$$

where  $r_0$  is the classical electron radius ( $2.818 \times 10^{-13}\ \text{cm}$ ),  $\rho_e$  is the electron density of the material or the total number of electrons per unit volume, and  $\lambda$  is the X-ray wavelength. The imaginary component of the refractive index stems from X-ray absorption, and  $\mu$  is the linear absorption coefficient of the material. For the  $1.5416\ \text{\AA}$   $\text{Cu-K}_\alpha$  X-rays used in this work, the surface reflection is practically independent of the polarization of the incident beam, *i.e.*, the p-wave and s-wave reflections are almost identical. For samples comprised of multiple elements,  $\rho_e$  can be expressed as:

$$\rho_e = N_a \rho_m \sum_i \frac{n_i Z_i}{A_i} \quad (3)$$



where  $N_a$  is Avogadro's number and  $n_i$  is the number fraction of the  $i^{\text{th}}$  element with atomic weight  $A_i$  and atomic number  $Z_i$ . Notice that converting  $\rho_e$  to the mass density  $\rho_m$  requires knowledge of atomic composition. If this composition is not known,  $n_i$  of thin films can be determined through a series of ion beam scattering experiments that include low energy forward scattering, traditional backscattering (*i.e.*, Rutherford backscattering), and forward recoil elastic scattering.<sup>[4a,20]</sup>

The optical constant  $\delta$  in Eq. (2) is typically on the order of  $10^{-6}$  for most materials. This means that the refractive index for X-rays is *slightly* less than unity, the refractive index of air or a vacuum. From Snell's Law, it is easy to demonstrate that for grazing incident angles  $\theta < \theta_c \approx (2\delta)^{1/2}$  the radiation is totally internally reflected. The extent to which the X-rays are reflected from the surface or interface at higher  $\theta$  depends upon the difference in electron densities  $\rho_e$  across the interface.

From an experimental perspective, reflectivity measurements are straightforward. Radiation impinges upon a film surface at a grazing angle  $\theta$ , and the intensity of reflected X-rays is measured at an equal angle  $\theta$ . Measuring the ratio of the reflected ( $I$ ) to the incident ( $I_0$ ) beam intensities (the so called reflectivity, which is usually presented on either logarithmic scale or as the logarithm of the ratio) down to  $I/I_0 = 10^{-8}$  is typically feasible with laboratory X-ray equipment, provided that low-noise (low background level) detectors are employed. X-ray reflectivity yields the Fourier transform of the electron density concentration gradient within the specimen. By nature of the inverse problem, this leads to inherent ambiguity in the interpretation in that more than one model concentration profile could describe the observed reflectivity. Therefore, it is always useful to use supporting information (and common sense) to corroborate the validity of the fitted interpretation.

### 1.C.1. Reflectivity from a Smooth Surface

Low-k dielectric films are typically supported on Si wafers. Therefore, single crystal Si is used herein for our example of reflectivity off a smooth substrate. Figure 2 displays theoretical SXR data as a function of the momentum transfer vector  $Q$  ( $Q = (4\pi/\lambda)\sin\theta$ ) from two Si surfaces, each with 1 Å (solid line) or 10 Å (dashed line) of surface roughness. This roughness is equivalent to a root mean square (RMS) value. However, within the context of SXR the surface roughness is not treated precisely since it can only be defined along the surface normal; the lateral nature of the roughness is ill-defined. Nevertheless, Figure 2 clearly illustrates that increased roughness diminishes the reflectivity, especially at high  $Q$ .

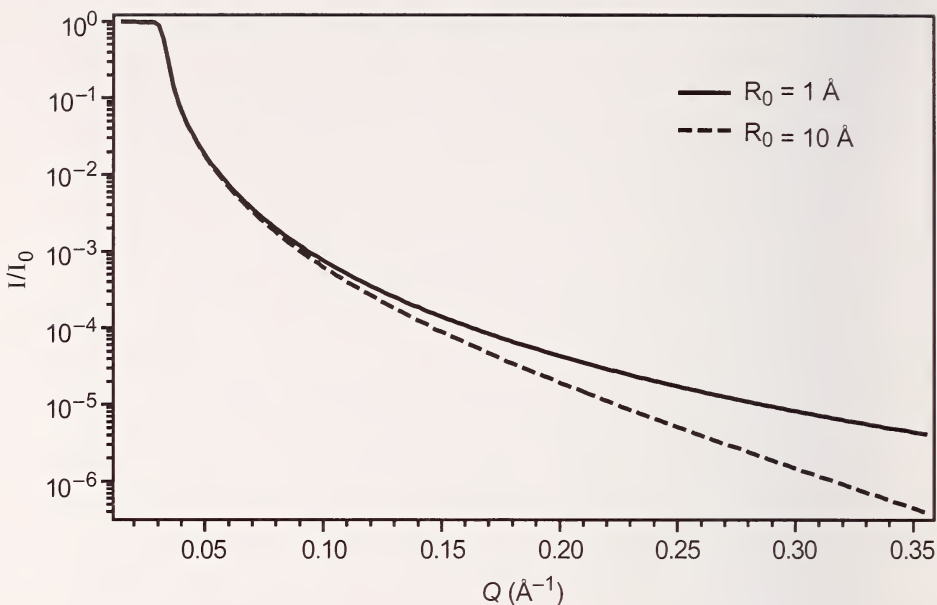


**Figure 2.** Calculated X-ray reflectivity results from silicon surface with different surface roughness. The solid and dashed curves correspond to RMS surface roughness values of 1 Å and 10 Å, respectively.

Notice that the position of the critical angle (where the reflectivity ratio rapidly decreases from 1.0) and the reflectivity data near the critical angle are largely unaffected by surface roughness. The corresponding  $Q$  at the critical angle  $\theta_c$  is defined as  $Q_c$ . The magnitude of  $Q_c^2$  relates to the total electron density  $\rho_e$  through the expression:

$$Q_c^2 = 16 \pi r_0 \rho_e \quad (4)$$

If this expression is recast in terms of angle  $\theta$ , rather than the wave vector  $Q$ , one obtains:

$$\theta_c = \lambda \sqrt{\rho_e r_0 / \pi} \quad (5)$$

Most materials display moderate X-ray absorption, even at wavelengths far from the absorption edges of their constituent elements. For Cu-K $_{\alpha}$  X-rays, Si has a linear absorption coefficient  $\mu = 1.47 \times 10^{-6} \text{ Å}^{-1}$ . Increasing  $\mu$  by a factor of 10 significantly affects the reflectivity data

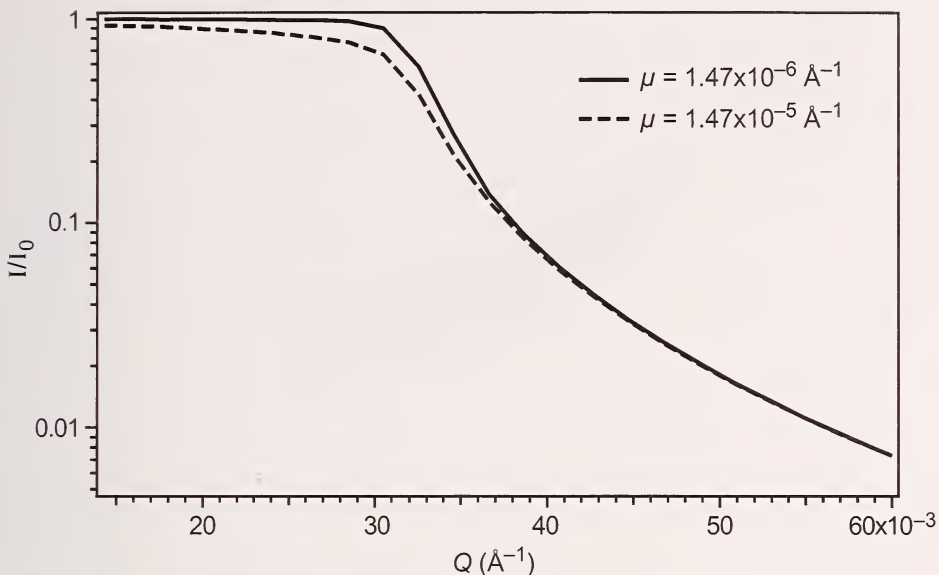


**Figure 3.** Calculated X-ray reflectivity data for Si surfaces with different linear absorption coefficients. The solid curve corresponds to a nominal absorption coefficient of  $\mu = 1.47 \times 10^{-6} \text{ \AA}^{-1}$  for pure Si, while the dashed curve indicates an order of magnitude increase,  $\mu = 1.47 \times 10^{-5} \text{ \AA}^{-1}$ .

as shown in Figure 3; the Si critical edge at  $Q = 0.032 \text{ \AA}^{-1}$  becomes less well-defined while the magnitude of reflectivity decreases in the low  $Q$  region. However, these effects become less noticeable at higher  $Q$ . Figure 3 illustrates the importance of incorporating the correct absorption coefficients in the data reduction and fitting algorithms. The reflectivity is relatively insensitive to small changes in  $\mu$ , but a factor of ten error leads to noticeable effects at low  $Q$ .

### 1.C.2. Reflectivity from a Thin Film on a Smooth Substrate

A thin polystyrene (PS) film is used to simulate the X-ray reflectivity data for the nanoporous thin films on Si substrates since the electron density  $\rho_e$  and absorption coefficient  $\mu$  are well documented. The  $\rho_e$  of PS is also comparable to the average  $\rho_e$  of most candidate low- $k$  materials. The  $\mu$  for PS will be slightly lower than most low- $k$  materials since the latter typically contain Si and O, elements with higher atomic absorptions than the C and H in PS. Nevertheless, PS is still an illustrative example, and Figure 4 shows the theoretical reflectivity for a smooth, 3000  $\text{\AA}$  PS film supported on a thick Si substrate. The main body of the figure emphasizes the low  $Q$  portion

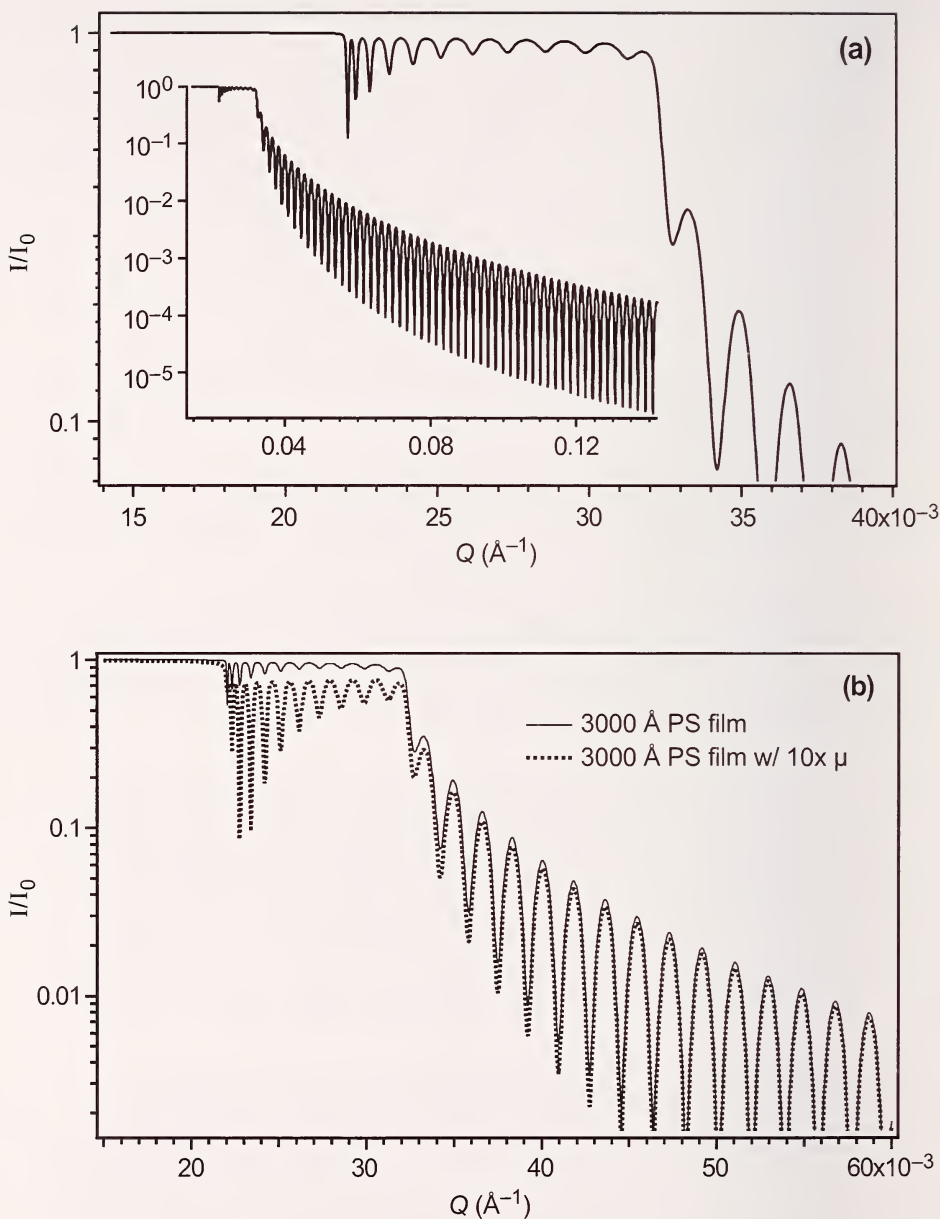


**Figure 4.** Part (a) displays the low  $Q$  theoretical X-ray reflectivity for a 3000  $\text{\AA}$  thick PS film supported on a Si wafer; the inset extends the reflectivity to high  $Q$ . The marked decrease in the reflectivity at  $Q = 0.022 \text{\AA}^{-1}$  and  $0.032 \text{\AA}^{-1}$  corresponds to the  $Q_c$  values of PS and Si, respectively. The region between these two  $Q_c$  values is the wave-guiding region of the reflectivity curve. Part (b) illustrates how a tenfold increase in the linear absorption coefficient  $\mu$  of the film significantly affects the reflected intensities in this wave-guiding region.

of the data while the inset of part (a) extends the  $Q$  range. Notice that the reflectivity goes through two sharp drops in intensity, first near  $Q = 0.022 \text{ \AA}^{-1}$  and then again near  $0.032 \text{ \AA}^{-1}$ . The latter drop is identical to those depicted in Figures 2 and 3, corresponding to the  $Q_c$  of the Si substrate. The drop near  $Q = 0.022 \text{ \AA}^{-1}$  corresponds to the  $Q_c$  of the PS layer. The  $Q_c$  of PS is smaller than the  $Q_c$  of Si, owing to the lower  $\rho_e$  of PS.

Multiple oscillations in the reflected intensity occur between the  $Q_c$ s of PS and Si, and a careful inspection reveals that the oscillations are not periodic; their frequency decreases towards higher  $Q$ . The physical origin of these oscillations is different from the high  $Q$  oscillations that occur with regular periodicity (discussed below). In the regime between these two  $Q_c$ s, the momentum transfer vector perpendicular to the film is sufficient for the X-rays to penetrate the air/film interface, but insufficient to penetrate the film/Si interface. Each minimum in this regime corresponds to an optical coupling condition, and the incident X-ray is transmitted via the thin film in a manner similar to an optical wave-guide. The phase and the amplitude of these oscillations relates to the electron density profile of the film. It is *imperative* to accurately fit data in this regime in order to obtain quantitatively correct information regarding the electron density profile of the film.

The absorption coefficient of the film plays an important role in shaping the reflectivity in this wave-guiding regime. As illustrated in Figure 4b, a tenfold increase of the PS absorption from  $\mu = 4.49 \times 10^{-8} \text{ \AA}^{-1}$  to  $4.49 \times 10^{-7} \text{ \AA}^{-1}$  dramatically decreases the reflectivity in the wave-guiding regime. The difference diminishes at high  $Q$ , similar to the effect seen in Figure 3. This reflects the fact that in the wave-guiding region, the incident beam is localized inside the film as an evanescent wave as opposed to simple transmission through the film at higher  $Q$ . The effective path length through the film in the wave-guiding region is significantly greater than the single reflection path that decreases in length at high  $Q$ , magnifying absorption effects in the former.

Beyond the  $Q_c$  of the Si, X-rays reflect from both the air/PS interface and the PS/Si interface. At periodic angles of incidence, the two reflected beams give rise to constructive and destructive interference patterns (oscillatory behavior) known as Kiessig fringes.<sup>[16–19]</sup> The total film thickness  $D$  is inversely proportional to the fringe periodicity  $\Delta Q$  ( $D \approx 2\pi/\Delta Q$ ). Fourier transform methods can also be used to convert the characteristic frequency of the Kiessig fringes into a thickness.<sup>[4g]</sup> More detailed structural information can further



be extracted from the SXR data, including the electron density as a function of distance from the substrate and the roughness of the film interfaces. However, these parameters must be obtained by systematically fitting various model electron density profiles to the reflectivity data. X-ray reflectivity data reduction and analysis are discussed later, but here it is important to appreciate that SXR can quantify thickness in films ranging from a few angstroms to approximately a micrometer thick, with angstrom-level resolution and without knowledge regarding the optical constants of the material.

## 2. EXPERIMENTAL

### 2.A. X-ray Reflectometer Requirements

Currently, there are several companies producing X-ray instruments capable of functioning as reflectometers. Some of these instruments are designed to function specifically as reflectometers, but it is also possible to use an X-ray diffractometer provided that the proper optics and degrees of freedom in sample positioning are available. In the following, we describe the necessary instrument requirements for high-resolution reflectivity experiments. SXR data are always collected with the grazing incident angle equal to the detector angle, as the term specular implies. (This *Recommended Practice Guide* does not address off-specular reflectivity, where the incident and detector angles are not equal. This can be used to probe lateral structure within the plane of the film<sup>[21]</sup>). Typical values for  $\theta$  in a reflectivity scan range from  $0.05^\circ$  to  $2.0^\circ$ , depending on the film thickness. The manner in which the incident and detector angles are maintained equal through the reflectivity scan depends upon the instrument. Conceptually, the simplest instruments maintain the sample flat (no sample tilt;  $\Omega = 0^\circ$ ) while the incident beam and detector simultaneously move through equal angles  $\theta$ . This scenario is illustrated schematically in Figure 5a. Other instruments are designed (primarily those which were intended to be diffractometers) with an incident beam that does not move. In this case, the specular condition is maintained by rotating the sample through an angle  $\theta$  while the detector simultaneously moves  $2\theta$ . In this  $\theta$ - $2\theta$  configuration, the sample tilt angle  $\Omega$  in Figure 5 effectively becomes  $\theta$ , while the detector angle becomes  $2\theta$ . For simplicity, the discussion herein uses the notation described in Figure 5a. However, extension to a  $\theta$ - $2\theta$  configuration is straightforward.

Alignment of the X-ray source ( $S$ ) and detector ( $D$ ) on the X-ray goniometer ( $G_x$ ) is crucial for reflectivity, more so than diffraction. The condition where  $S$  is focused directly at  $D$  defines the  $\theta = 0^\circ$  state, and the beam must pass precisely (within a few  $\mu\text{m}$ ) through the origin of the  $G_x$  under these conditions (see Figure 5b). This condition is not automatically achieved or ensured with a factory-aligned diffractometer. It is not trivial to ensure that  $D$  and  $S$  are focused perpendicular to the tangent of the goniometer circle  $G_x$  (i.e., at the origin  $O$ ). Most instruments provide angular degrees of freedom such as  $\alpha$  (see Figure 5b) to change the incident (source) or acceptance (detector) angles relative to a tangent of  $G_x$ . This leads to the potential situation  $S'D'$  where the detector and source are directly focused at each other, but the X-ray beam does not pass through the origin. Defining  $S'D'$  as  $\theta = 0^\circ$  would



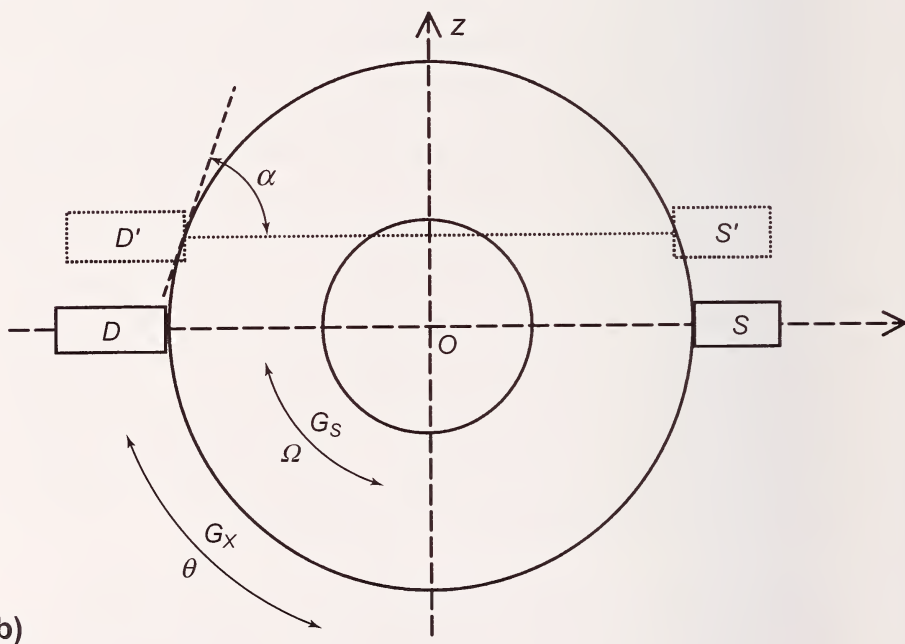
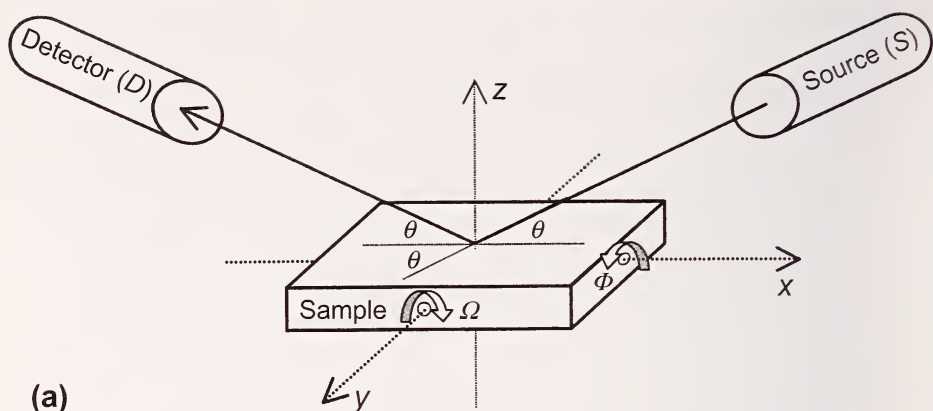


**Figure 5.** The diagram in part (a) depicts the relevant degrees of freedom for an X-ray reflectometer. In this representation,  $\theta$  defines goniometer angles for both the incident X-ray beam and the detector position (X-ray optics) while  $\Omega$ ,  $\Phi$ , and  $z$  are the tilt, yaw, and vertical translation ( $x$  and  $y$  would be the lateral translations) of the sample stage. The X-ray goniometer and sample stage move/rotate on separate goniometers,  $G_x$  and  $G_s$  respectively, as shown in part (b), and it is advisable to make these circles concentric. It is critical that the X-ray beam passes through the center  $O$  of the  $G_x$ ; detector and X-ray source positions  $D'$  and  $S'$  where the beam does not pass through the origin are unacceptable, as discussed in the text.

lead to incorrect angular values of the goniometer. In a diffractometer, this type of misalignment is corrected by measuring the diffraction from a known crystal. The various degrees of freedom ( $\alpha$  and  $\theta$ ) are adjusted until the experimentally obtained diffraction peaks coincide with the theoretical values. However, this level of alignment is usually insufficient for reflectivity measurements. The positions of the high  $Q$  diffraction peaks are not extremely sensitive to the X-ray beam passing through the origin; further refinements in the alignment of the X-ray optics are usually required.

For the  $\theta$ - $\theta$  instrument depicted in Figure 5, the process of focusing the incident beam precisely through the center of  $G_x$  is non-trivial and typically requires fabricating a non-standard alignment device. Such a device might operate on the fact that a tightly collimated beam (either ribbon or pin-hole) of X-rays focused at the origin of  $G_x$  will not move laterally across a flat surface (if that surface also passes through the origin of  $G_x$ ) when the incident  $\theta$  is scanned over large angles. The position of the beam can be visualized using a phosphorous screen, photographic film, or a 2-D detector array. Typically, the large flat surface is brought into the beam at  $\theta = 0^\circ$  near the origin  $O$  and rotated about the sample stage goniometer ( $G_s$ ) until the plane of the film lies parallel to the X-ray beam (the process by which this is done is described below in reference to Figure 8, parts (a) through (c)). With the sample plane and beam now coplanar, the incident  $\theta$  is scanned over a large range (*i.e.*,  $10^\circ$  through  $90^\circ$ ). If the beam is focused off the center of the  $G_x$ , the point of focus will move across the flat surface with  $\theta$ . If this is the case, the angle  $\alpha$  on the incident X-ray source is adjusted in the appropriate direction, and the process is repeated until the beam trace does not move with  $\theta$ . For  $\theta$ - $2\theta$  instruments, the alignment is easier if the sample goniometer can be rotated by  $180^\circ$  (this is usually not possible in  $\theta$ - $\theta$  instruments). In this scenario, the  $\theta = 2\theta = 0^\circ$  condition that passes through the origin of the goniometer can be tested by moving a knife edge on the sample stage into the beam until it cuts the intensity in half (similar to Figure 8b, discussed later). If the focus point is at the origin, rotating the sample by  $180^\circ$  results in the same final intensity as the sample moves from blocking the bottom half of the beam to the top half; it should be symmetric.

For specular reflectivity, it is not critical that the centers of  $G_x$  and  $G_s$  coincide. As long as (i) the beam passes directly through the origin of  $G_x$ , (ii) the sample surface is coplanar with the beam at  $\theta = 0^\circ$ , and (iii) the incident beam can be focused onto the sample, small off-sets of  $G_x$  and  $G_s$  will not significantly affect the X-ray reflectivity. However, it is advisable to make  $G_x$  and  $G_s$  as concentric as possible since off-sets will make the angles in rocking curves ( $\Omega$  rotations, sometimes used in

off-specular reflectivity) inaccurate. Likewise, this would also affect the footprint correction that is discussed below. The procedure by which  $G_x$  and  $G_y$  are made concentric is non-trivial and beyond the scope of this Practice Guide, but it is similar to focusing the incident beam through the origin of  $G_x$ .

The resolution of an X-ray reflectometer depends upon both the angular resolution of the goniometers that move the incident beam/detector and the quality of the beam conditioning optics. Since the periodicity of the Kiessig fringes varies inversely with film thickness, a greater resolution is required to measure thicker films. As a practical upper bound, it is not possible to quantify films thicker than a few micrometers using a fine focus copper X-ray tube. A standard X-ray diffractometer utilizing a  $\text{Cu-K}\alpha$  radiation filter through a Ni foil filter, a detector with a 100 eV band pass filter to crudely discriminate the  $\text{Cu-K}\alpha$  reflections, and simple Soller slit pack collimation (standard on most base-model diffractometers) on the incident and reflected beams should be able to generate reflectivity curves on films 1000 Å to 2000 Å thick. To measure reflectivity from thicker films requires non-standard upgrades or additions to increase the resolution. We recommend conditioning the incident  $\text{Cu-K}\alpha$  beam with a four-bounce germanium (Ge [220]) monochromator. It is also helpful to further condition the reflected beam with a three-bounce germanium Ge [220] channel cut crystal. This configuration ensures that only specularly reflected X-rays are detected (more so than 100 eV band pass filter), and results in a  $\text{Cu-K}\alpha$  beam with a fractional wavelength spread of  $1.3 \times 10^{-4}$  and an angular divergence of  $6 \times 10^{-5}$  rad (12 arc seconds). The motion of the goniometer arms that control the incident beam and detector position should also be highly accurate. Using a closed-loop active servo control system, an angular reproducibility of  $0.0001^\circ$  should be attainable. Utilizing these high precision settings in both the X-ray optics and the goniometer control, one should be able to detect the very narrowly spaced interference fringes from films on the order of 1 μm thick.

For an SXR measurement, it is recommended to cover as wide a  $Q$  range as possible to increase the confidence in model fits to the data. A wide  $Q$  range also facilitates quantifying exceedingly thin films whose Kiessig fringes become widely separated in  $Q$  space. This often necessitates obtaining reflectivities as low as  $10^{-8}$ . Given that the typical incident beam flux is approximately  $10^7$  counts/s for most laboratory instruments with a highly monochromated and tightly collimated beam, the photon flux at the detector is often 1 count/s or less. Therefore, the X-ray detector must have extremely low noise or “dark current” levels, preferably far below 1 count/s. Enhanced intensities can be gained by incorporating a focusing mirror in the incident beam, effectively

directing a greater number of X-rays into the four-bounce Ge [220] monochromator. Depending on the noise level of the detector, it should be feasible to quantify the thickness in films as thin as (25 to 50) Å using SXR. However, the density and roughness measurements are very difficult in such thin films. There are so few Kiessig fringes (in these thin films) that it is impossible to establish the high  $Q$  decay behavior that is related to film roughness. Likewise, the significantly reduced path length, even in the wave-guiding region, leads to negligible absorption or an inability to resolve the critical edge of the film. The X-ray reflectometer used in our laboratory contains all of the resolution-enhancing components described above, including the four-bounce and three-bounce Ge [220] monochromators, the focusing mirror, the low-noise detector, and the closed-loop active servo control goniometer positioning.

### 2.A.1. Resolution Effects

The thickness of most low- $k$  films range from 100 nm to 1  $\mu\text{m}$ . For a 1  $\mu\text{m}$  thick film, the spacing between interference fringes will be approximately  $6 \times 10^{-4} \text{ \AA}^{-1}$  beyond the wave-guiding regime. However, the spacing between the first few oscillations in the wave-guiding region is even smaller, as demonstrated in Figure 4. This imposes very stringent requirements on both the wavelength dispersion and angular divergence of the instrument in addition to the step size of the goniometer. To resolve interference fringes with a spacing of  $6 \times 10^{-4} \text{ \AA}^{-1}$  requires approximately 10 data points within the  $Q$  range of a single fringe. This corresponds to a minimum repeatable angular step size of approximately  $0.0004^\circ$ . Angular divergence is also critical in defining the resolution of the reflectometer, as shown in Figure 6; the theoretical SXR reflectivity curves for a smooth, 1  $\mu\text{m}$  PS film on Si at three different angular divergences are given. The solid line corresponds to  $\delta\lambda/\lambda = 6 \times 10^{-5}$  with an angular divergence of  $\delta\theta = 3 \times 10^{-5} \text{ rad}$ , while the dashed and dotted lines indicate angular divergences increased by  $\times 2$  and  $\times 4$ , respectively. The angular divergence of  $6 \times 10^{-5} \text{ rad}$  is appropriate for instruments used in our laboratory and the reflectivity data presented in this guide. Figure 6a indicates that angular divergence has a large impact on the reflectivity in the low  $Q$  wave-guiding regime; the first few oscillations right above the  $Q_c$  for PS become almost indistinguishable at  $\delta\theta = 6 \times 10^{-5} \text{ rad}$  ( $\times 2$ ). At  $\delta\theta = 1.2 \times 10^{-4} \text{ rad}$  ( $\times 4$ ) the oscillations nearly disappear. In Figure 6b, one can see that the amplitude of the interference fringes in the high  $Q$  regime are also dampened with increasing angular divergence, but to a lesser extent in comparison to the low  $Q$  regime.



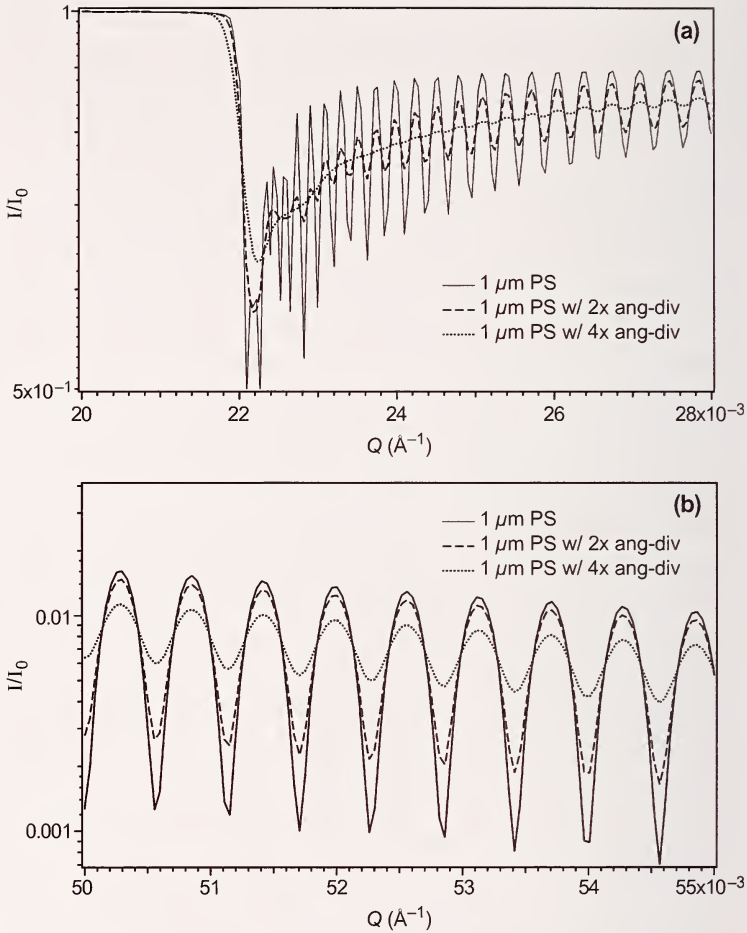


**Figure 6.** Calculated X-ray reflectivity curves for a 1 μm PS film with instrumental angular divergences of  $(3 \times 10^{-5}, 6 \times 10^{-5}$  and  $1.2 \times 10^{-4})$  rad in both the wave-guiding (part a) and high  $Q$  (part b) regimes. Increasing angular divergence significantly damps the interference fringes, especially at low  $Q$  within the wave-guiding regime.

The wavelength dispersion of the instrument also plays a critical role in the quality of the SXR data, similar in effect to the angular divergence. Figure 7 shows the theoretical X-ray curves for the 1 μm thick PS film with wavelength divergences of  $\delta\lambda/\lambda = 6 \times 10^{-5}$  (solid lines) and  $\delta\lambda/\lambda = 6 \times 10^{-4}$  ( $\times 10$ , dotted lines), both with an angular divergence of  $\delta\theta = 6 \times 10^{-5}$  rad. The wavelength dispersion of our reflectometer,  $\delta\lambda/\lambda = 1.3 \times 10^{-4}$ , is intermediate between the two values depicted in Figure 7. Greater wavelength dispersions tend to dampen the amplitude of all the oscillations throughout the entire  $Q$  region. The simulation

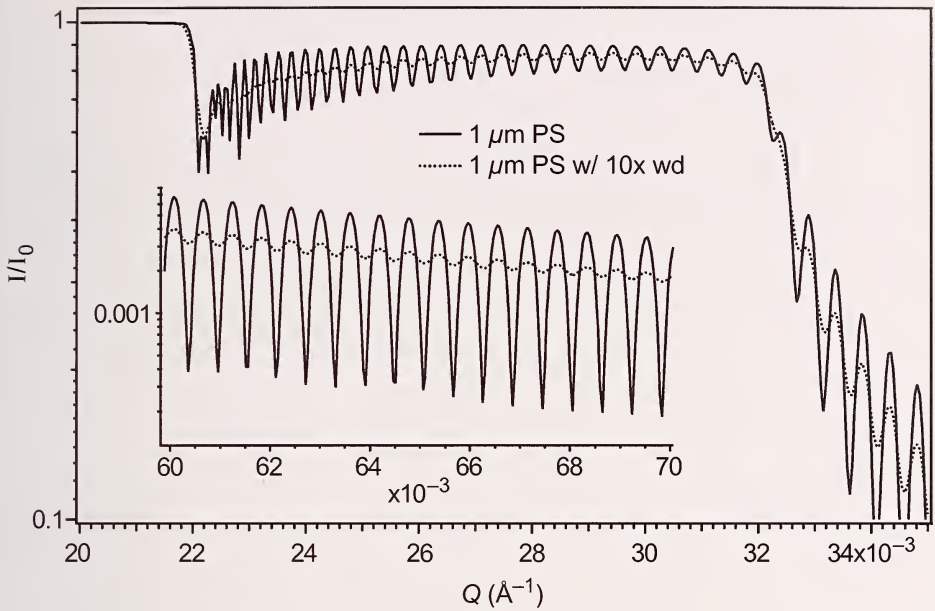


**Figure 7.** Theoretical X-ray reflectivity curves for a  $1\ \mu\text{m}$  PS film with two different wavelength dispersions. The solid line corresponds to a wavelength dispersion ( $wd$ ) of  $\delta\lambda/\lambda = 6 \times 10^{-5}$  while the dotted line denotes  $\delta\lambda/\lambda = 6 \times 10^{-4}$ . The main body illustrates these effects in the low  $Q$  wave-guiding region while the inset emphasizes the high  $Q$  effects.

in Figure 7 is based on an instrument with a four-bounce Ge [220] monochromator on the incident beam. Adding the three-bounce Ge [220] to the reflected beam will increase the resolution but only marginally. Replacing these Ge optics with a single crystal Si-based monochromator can further enhance the wavelength resolution, but this comes at the price of a decreased photon flux.

## 2.A.2. Recommended Procedure for Sample Alignment

It is always critical to precisely align the sample in any SXR or XRP experiment. The first requirement is that the sample is flat with a mirror-like surface. A RMS surface roughness greater than  $100\ \text{\AA}$  will degrade the Kiessig interference fringes to the point where XRP is not possible. Likewise, large-scale bowing or curvature in the sample is undesirable as this leads to different regions of the film being “aligned” at different angles. Since the footprint of the illumination in a reflectivity experiment is large, the sample should be flat over an

area of several  $\text{cm}^2$ . Once the flat sample is mounted into the X-ray reflectometer, the optics need to be aligned. This is described below with the help of Figure 5 which describes the requisite degrees of freedom for a typical reflectometer.

The first step is to determine the  $\theta = 0^\circ$  condition for the reflectometer. The procedure described below is predicated on the assumption that

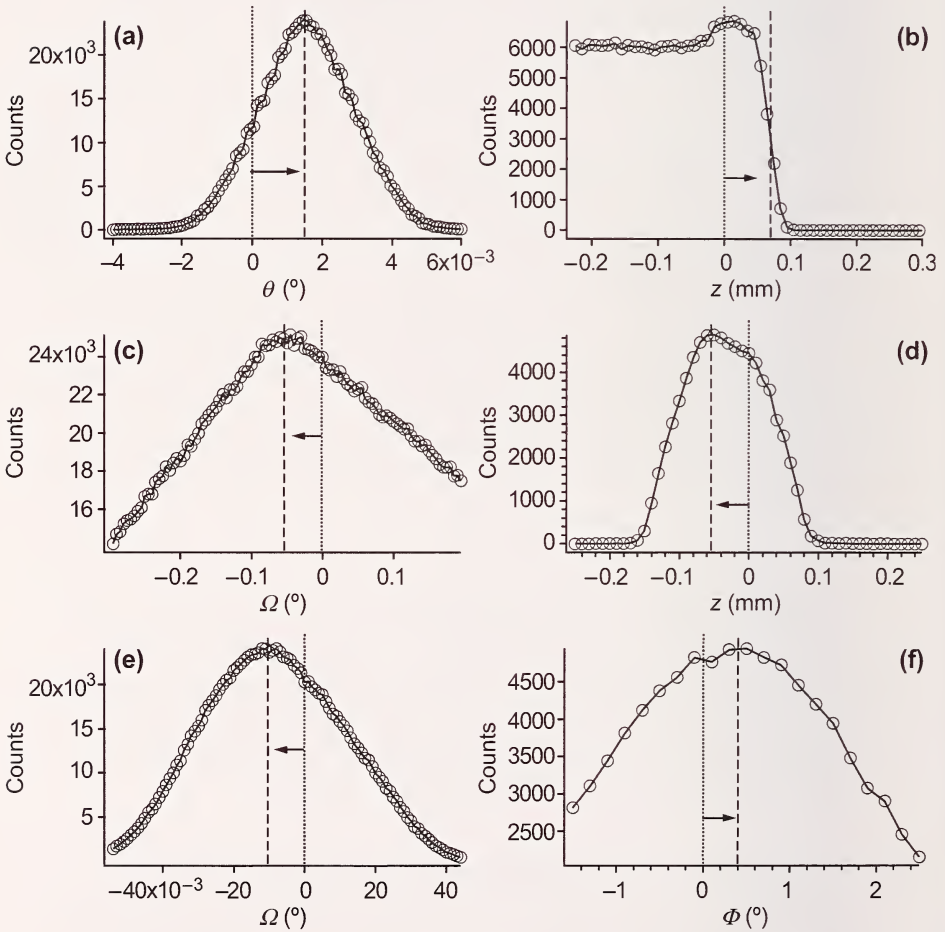


**Figure 8.** Panels (a) through (f) illustrate the process required to align the X-ray reflectometer, as described in the text. In each panel, the dotted vertical line indicates the current zero position for each degree of freedom while the dashed line indicates the new position that should be reinitialized to zero. Data are presented for illustrating the alignment procedure only, so the standard uncertainties are irrelevant and not provided.



X-ray optics are calibrated such that at  $\theta = 0^\circ$  the beam passes precisely through the origin of the goniometer  $G_x$ . Lower the sample height in the  $z$  direction sufficiently so that the sample is not in the beam. Then scan the range of  $\theta$  values on either the incident or reflected beam (scanning only one while the other is maintained stationary) until a maximum intensity is achieved (see Figure 8a). This maximum corresponds to the condition where the X-ray source is focused directly at the detector. According to Figure 8a,  $\theta$  needs to be offset by approximately  $0.0014^\circ$  so that the  $\theta = 0^\circ$  position corresponds to the actual peak intensity (indicated by the shift from the dotted to dashed lines). The mechanism by which this scan is achieved may differ slightly between reflectometers. In some units the position of the X-ray source is fixed and the detector moves. In this situation  $\theta$  is half the angle that the detector moves, defining a  $2\theta$  scan. In other units the source and detector move in concert, each by an amount  $\theta$ , in what is known as a  $\theta$  scan. As a word of precaution, these scans to determine the zero angle should be done with an understanding of the intensity limits of the detector. At full power (typically on the order of 40 mA at 40 kV for most laboratory X-ray sources), the X-ray flux is often sufficient to saturate the detector and induce irreversible damage. It is prudent to locate the  $\theta = 0^\circ$  condition at a reduced power setting on the X-ray generator or with an attenuator inserted in the X-ray beam.

After the  $\theta = 0^\circ$  condition is determined, the stage should be scanned in the  $z$  direction until the sample enters the beam. This will be obvious by the rapid decrease in the count rate on the detector as shown in Figure 8b. Drive the sample into the beam up to the point where the count rate is cut in half as compared to the open beam, and tentatively assign this position as  $z = 0$ . In Figure 8b, the current  $z = 0$  position (dotted line) needs to be shifted up by 0.075 mm to coincide with the physical beam center (dashed line). Now scan  $\Omega$  about its current position over a sufficiently large range (typically an angular range greater than  $0.5^\circ$ ). If the plane of the sample surface is parallel to the vector between the source and the detector at  $\theta = 0^\circ$ , this scan produces a maximum intensity at the position approximately  $\Omega = 0^\circ$ . If the maximum does not coincide with the  $\Omega = 0^\circ$ , *i.e.*, dotted line in Figure 8c, drive  $\Omega$  to the position of the maximum (dashed line), and set this new position as  $\Omega = 0^\circ$ . In Figure 8c, this corresponded to a  $\Omega$  shift of  $-0.05^\circ$ . It is possible that the  $\Omega$  scan in Figure 8c does not reveal a maximum, rather the intensity increases or decreases monotonically. This indicates that a larger angular range of  $\Omega$  is needed for the scan. It is also possible,

and likely, that a larger  $\Omega$  scan also tilts the sample out of the beam. This is indicated by a plateau in the intensity rather than a maximum. In this case, drive  $\Omega$  to the highest intensity, somewhere in the plateau region. Then increase the sample height until the open beam intensity is cut in half, and repeat the  $\Omega$  scan. It is not uncommon to go through several iterations of these sample height adjustments and  $\Omega$  scans before the  $\Omega = 0^\circ$  condition is located, especially the first time a new sample is mounted.

At this point the sample is crudely aligned. To fine-tune the alignment, it is necessary to increase  $\theta$  (both source and detector) to a sub-critical value where total reflection of the incident X-rays occurs. For most polymer or low-k dielectric films  $\theta = (0.1^\circ \text{ to } 0.2^\circ)$ , or  $2\theta = (0.2^\circ \text{ to } 0.4^\circ)$ , is sufficient to achieve these sub-critical conditions. At these specular reflectivity conditions there should be a moderate intensity reaching the detector. If the power was reduced or attenuators placed in the beam at  $\theta = 0^\circ$ , it is now safe to undo these precautions. Fine-tuning the alignment is an iterative process of systematically adjusting  $z$ ,  $\Omega$ , and  $\Phi$ . We typically start by scanning  $z$  over a range of 0.2 mm to 0.4 mm about the current position as shown Figure 8d. If the current  $z = 0$  position (dotted line) does not correspond to the pronounced maximum (dashed line), drive  $z$  to the maximum intensity, and reset this position to  $z = 0$  (an offset of  $-0.05$  mm in Figure 8d). If no maximum is observed it is necessary to increase the range, but this should generally not be the case if the crude alignment described above is done correctly. Once the maximum in  $z$  is found, scan  $\Omega$  about its current position over a range of approximately  $0.05^\circ$ . Notice that this range is significantly smaller than the previous range of  $0.5^\circ$  recommended at  $\theta = 0^\circ$ ; the  $\Omega$  scan is considerably more sensitive at these specular reflectivity conditions. This scan should produce a strong, sharp peak as shown in Figure 8e. Once again, if the  $\Omega = 0^\circ$  (dotted line) does not correspond to the maximum (dashed line), reset  $\Omega$  to the proper zero (shift of  $-0.010^\circ$ ) and proceed to maximize  $\Phi$ . We recommend scanning  $\Phi$  over a large range of  $3^\circ$  as shown in Figure 8f. Do not expect a pronounced maximum since this is the least sensitive of the alignment adjustments. As shown in Figure 8f, the angle  $\Phi = 0^\circ$  needs to be offset by  $0.4^\circ$  to properly align the reflectometer. The fine-tuning procedure described in this paragraph should be reiterated several times until the peak positions no longer change between successive iterations; in the notation of Figure 8 this means that the dashed and the dotted vertical lines coincide. When this condition is achieved, initialize  $\Omega = \Phi = z = 0$ , and the reflectometer is ready for a measurement.

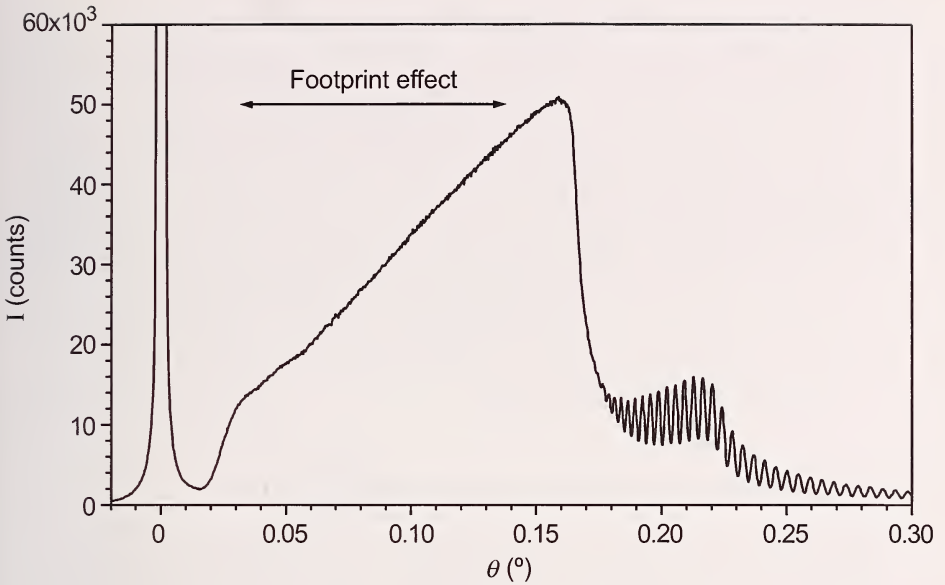


**Figure 9.** A  $\theta$  scan of a well-aligned reflectometer. The pronounced peak (off the vertical scale of the plot) from the main beam defines the  $\theta = 0^\circ$  condition. The linear increase in intensity with the angle beyond the main beam peak comes from increasing the fraction of the beam that is focused onto the sample (footprint effect). Standard uncertainty in the intensity is less than the line width.

Figure 9 displays a  $\theta$  scan for a well-aligned reflectometer. The intense peak of the main beam defines the zero angle condition where  $\Omega = \theta = 0^\circ$ . Beyond the main beam peak, the reflected intensity increases linearly with  $\theta$  because of changes in the area of the X-ray beam footprint with angle. The beam height at grazing incidence angles geometrically leads to large variations in the exposed film area (footprint effect). At very shallow incident angles, the aerial footprint of the X-rays can illuminate an area that is larger than the area of the sample. As  $\theta$  increases, the area of this footprint decreases, and more X-rays are focused onto the aligned sample. This results in an increase of the reflected intensity with  $\theta$  from purely geometric considerations. In the section below, we describe how the reflectivity curves must be corrected for this footprint effect before proper interpretation of fits to the data can be carried out. As  $\theta$  continues to increase, the critical angle of the sample is eventually reached, and the X-rays start to penetrate the films, giving rise to the pronounced decrease in the reflected intensity and the onset of the fringes.

Realignment of the reflectometer between successive measurements is sometimes required, depending on several factors. The first is the stability of the goniometers. If the motors that move the sample and/or the goniometer tend to drift, frequent alignment will be required. If the temperature of the stage is varied, thermal expansion is often sufficient to require readjustments of the sample height. Typically, the infusion of adsorbents inside the pores does not require realignment provided that the positioning motors are stable and the sample exhibits minimal swelling ( $< 1\%$  in thickness). We generally recommend noting the count rate at a sub-critical angle like  $\theta = 0.1^\circ$  and  $\Omega = \Phi = \chi = 0$ . If this count rate decreases by more than  $10\%$  at any point, we recommend sample realignment.

## 2.B. Methods of Partial Pressure Control

XRP is predicated on the ability to control the partial pressure of an organic solvent in the sample environment. There are several ways in which this environmental control can be achieved. We discuss three such methods below and comment on their attributes and liabilities. These techniques include: (i) the controlled isothermal mixing of solvent-free and vapor-saturated carrier gases; (ii) sample temperature variations in a vapor saturated carrier gas; and (iii) pure solvent vapor exposure. We demonstrate these ideas using toluene as a model organic vapor but emphasize that any number of different organic solvents can also be employed.

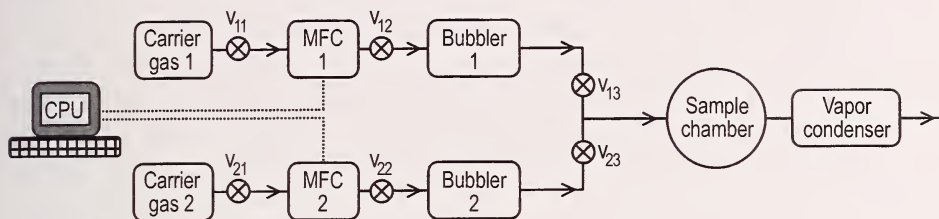
### 2.B.1. Isothermal Mixing with Carrier Gases

The  $P/P_0$  ratio can be varied to probe a range of  $r_c$  values through a controlled, isothermal mixing of streams of pure ( $P/P_0 = 0$ ) and toluene-saturated ( $P/P_0 = 1$ ) carrier gas. Figure 10a schematically indicates the construction of such a device. We typically use dry air for carrier gases 1 and 2. Using 6.35 mm (1/4 inch) stainless steel tubing (other gages can be utilized) and standard Swagelok<sup>[22]</sup> fittings, we connect the air cylinders to mass flow control (MFC) valves. We utilized MKS Instruments 1179A MFC valves configured for a maximum flow rate of 500 standard  $\text{cm}^3/\text{min}$  (sccm). The size of the sample chamber, the desired speed of the system, and the size of the tubing primarily determine the maximum flow rate. If the flow rate is too high relative to the conductance of the system, the carrier gas will pressurize the system and affect the equilibrium partial pressure. For a similar environmental control set-up for our smaller neutron scattering



## Environmental Control Methods

### (a) Mixed carrier gases



### (b) Pure solvent vapor

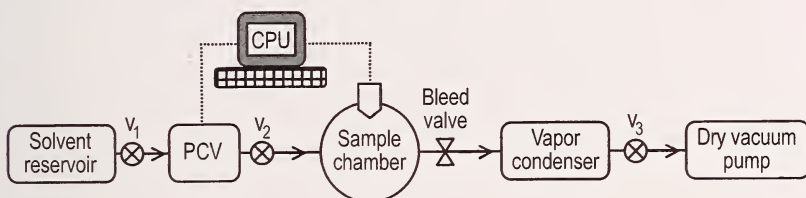


**Figure 10.** Schematics depicting the different methods by which the partial pressure in the XRP sample chamber can be controlled. Part (a) is based on bubbling a carrier gas through a solvent reservoir while part (b) illustrates controlled flow of pure vapor into a chamber that is continually being evacuated by a vacuum pump.

sample cells, 1.59 mm (1/16 inch) stainless steel tubing is used, and the total flow rate is reduced to 10 sccm in order to prevent pressurization. It is recommended that the MFCs be fitted with stainless steel valve seats. Care should be taken to ensure that the wetted surfaces of the control apparatus are compatible with the solvent vapors being used. The flow rates of our MFC valves are computer controlled through a MKS Instruments 146C unit configured with two MFC cards. After passing through the MFC valves, the carrier gas streams are fed into bubblers that contain the solvent of interest. In our system, 500 cm<sup>3</sup> stainless steel bubblers from Epichem (Model 212, ordered “empty”) with liquid level sensors were utilized. Other sizes or standard glass bubblers can be used; we opted for stainless steel after breaking several glass bubblers in prototype controllers. After the air streams pass through the two the bubblers, they are mixed together and enter the X-ray reflectometer sample chamber. This chamber is in a vacuum-tight aluminum housing, sealed with a Viton o-ring, and has X-ray transparent beryllium windows to allow the X-rays to enter and exit.



There are also two ISO-25 QF ports that allow the carrier gas to enter one side of the chamber, flow across the sample, and then exit on the other side of the sample. Far downstream on the exit line, the toluene vapor is removed from the carrier gas with a Kinetics Thermal System VT890A cold trap. Finally, notice in Figure 10 the manual shut off valves inserted between all components. These are useful in preventing unwanted back-flow of organic vapors or cross-contamination between the two carrier gas lines when the system is static.

The operation of the system illustrated in Figure 10a is straightforward. Bubbler 1 is typically left empty (dry air) while bubbler 2 is filled with approximately 250 cm<sup>3</sup> of toluene. Using the 146C control unit, the two MFC valves are set in the "totaling mode" for a 100 sccm total flow rate. In the totaling mode, a flow rate is manually entered for the independent MFC channel (arbitrarily chosen to be the dry air), and the flow rate for the dependent MFC (in this case the toluene) is automatically adjusted to total 100 sccm. For example, if a flow rate

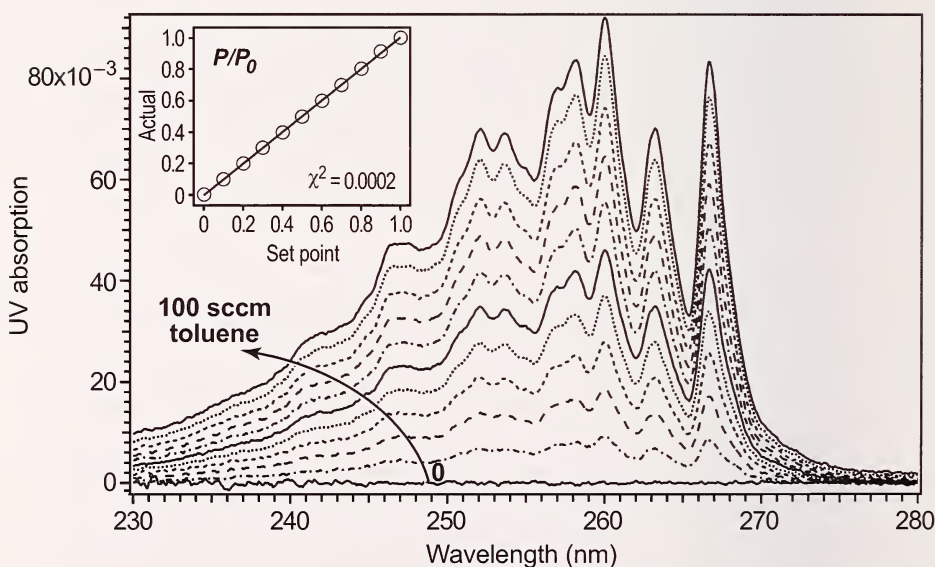


**Figure 11.** UV absorption spectra of mixtures of pure and toluene-saturated air with a total flow rate of 100 sccm. Starting with the flat featureless spectra showing nearly 0 absorbance (pure airflow), each successive curve indicates a 10 sccm increment in the flow rate of the toluene-saturated air and a 10 sccm decrement in the pure airflow rate. The ratio of the integrated areas between the curve of interest and the toluene-saturated curve, using the pure air curve as a baseline, defines  $P/P_0$ . The inset shows a linear correlation between the desired set-point and the measured  $P/P_0$ , with a least-squared deviation of  $\chi^2 = 0.0002$ .

of 35 sccm is entered for the dry air, the toluene line automatically adjusts to 65 sccm to give a total flow rate of 100 sccm and a toluene partial pressure of  $P/P_0 = 0.65$ . By varying the dry air flow rate from 0 sccm to 100 sccm,  $P/P_0$  values from 1 to 0 can be achieved.

We generally find that this controlled mixing of dry and toluene-saturated air provides adequate partial pressure control. This is based on two separate control experiments. First, the XRP data we obtain using a toluene flow rate of 100 sccm ( $P/P_0 = 1.0$ ) is identical to the data from a static system where the sample chamber is sealed with an open beaker of toluene inside the chamber. Second, we have performed separate experiments to corroborate that the partial pressures are accurate at set-points where  $P/P_0 < 1.0$ . Toluene has a strong ultra-violet (UV) absorption between 230 nm and 280 nm, as shown in Figure 11. The integrated absorption in this regime, in reference to the dry air spectrum, defines the partial pressure.

Figure 11 shows a series of UV absorption spectra for toluene flow rate of 0 sccm to 100 sccm, in 10 sccm increments, using the totaling mode of operation where the total flow rate is 100 sccm. In this experiment, the mixed gas line was connected not to the X-ray reflectometer, but used to purge the sample cell of a Perkin Elmer UV spectrometer. The partial pressures were calculated from the integrated absorption between 230 nm and 280 nm, and the inset of Figure 11 shows an excellent correlation between measured  $P/P_0$  and the set-point. The data fit to a linear function with a slope of  $1.008 \pm 0.004$ , intercept of  $-0.005 \pm 0.002$ , and  $\chi^2 = 0.0002$ .

It is critical to control the temperature of the sample stage since variations, under certain circumstances, can affect dramatic changes in the adsorption behavior; typical room temperature fluctuations of a few degrees can lead to irreproducible results. We typically operate at a set point of 25.0 °C, and thermal fluctuations in the sample stage of less than  $\pm 0.1$  °C are sufficient to achieve smooth isotherms with minimal fluctuations. We also recommend regulating the temperature of the bubblers since evaporation cools the toluene. The equilibrium vapor pressure is temperature dependent, and cooling the toluene will lead to decreased levels of saturation. Our system circulates water maintained at 25 °C around the exterior of the bubblers to prevent cooling. The sample stage and bubbler are the only components of our system that are temperature controlled. Efforts were not made to regulate the temperature of the gas handling lines, air supplies, etc. simply because adequate data was obtained (see Figure 11) without such precaution. This, however, may not be true under all conditions.

If the sample is heated above ambient, it would also be necessary to heat all the components in the vapor handling system. Otherwise, toluene vapor would condense on the ambient (cooler) surfaces, decreasing the partial pressure of the environment at the sample. Likewise, large temperature fluctuations in the environment or possibly the use of other solvents may require more extensive thermal regulation.

## 2.B.2. Sample Temperature Variations in a Vapor-Saturated Carrier Gas

Two thermodynamic parameters in Eq. (1), either  $T$  or  $P$ , can be used to vary the critical radius for capillary condensation. In the preceding section, we described how different values of  $r_c$  can be probed isothermally by mixing streams of dry and toluene-saturated air (from here on we refer to this as the “ $P$  variation method”). Analytically, this isothermal method is attractive since both  $\gamma$  and  $V_m$  are constant. However, the experimental set-up for isothermal mixing can be somewhat elaborate since accurate mass flow control valves are required. It is easier to simply flow a stream of air saturated with toluene at ambient temperature over the sample and then vary film temperature (referred to as the “ $T$  variation method”). When the film is also at ambient temperature,  $P/P_0 = 1.0$  (where  $P$  is current vapor pressure of the toluene in the atmosphere and  $P_0$  is the equilibrium vapor pressure), and toluene condenses in all of the accessible pores. If the sample is heated, the equilibrium vapor pressure  $P_0$  of the condensed toluene increases, but the toluene content in the airstream (*i.e.*,  $P$ ) remains the same because it was equilibrated at room temperature. This effectively reduces  $P/P_0$  and thereby  $r_c$ . This non-isothermal approach is complicated by the fact that the temperature dependence of  $\gamma$  and  $V_m$  need to be accounted for. From a thermodynamic perspective, though, it is immaterial whether  $T$  or  $P$  is used to probe the range of critical pore sizes; the two should yield identical pore size distributions. However, we demonstrate later that this is not always the case.

Figure 12 graphically illustrates how the  $T$  and  $P$  variation methods probe a range of  $r_c$  values from approximately 1 Å to 250 Å when toluene is used as the condensate vapor. The vertical axis indicates the critical radius  $r_c$  while the upper and lower horizontal axes correspond to the  $P$  and  $T$  variation methods, respectively. The solid line (reading from the upper horizontal axis) shows how  $r_c$  varies isothermally (20 °C) with  $P/P_0$ , achieved by mixing dry and

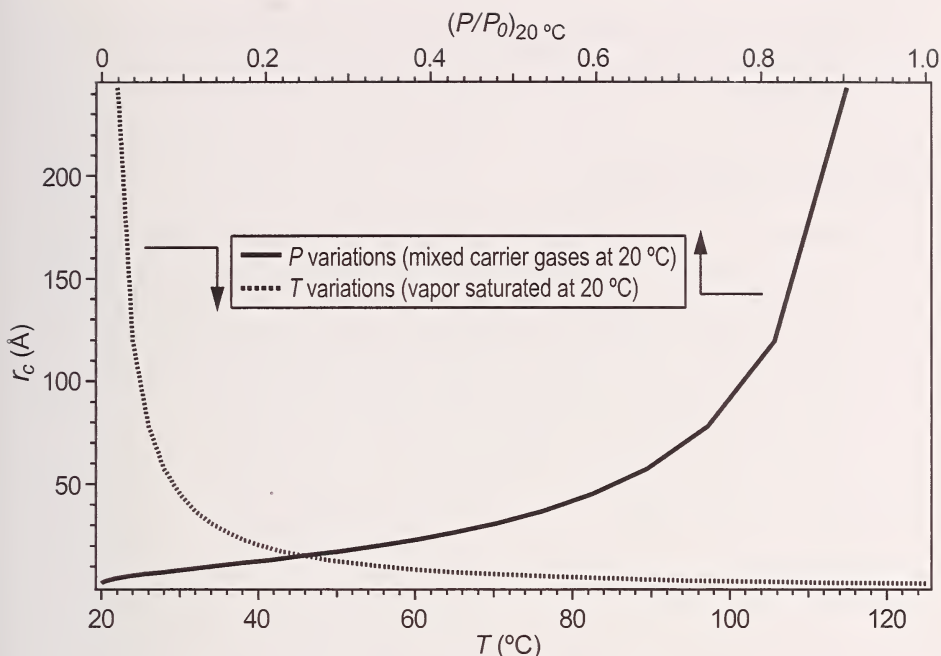


**Figure 12.** There are two ways in which  $r_c$  can be varied in the Kelvin equation.  $r_c$  values from approximately (1 to 250)  $\text{\AA}$  can be obtained by mixing ratios of dry and toluene-saturated air at  $20\text{ }^\circ\text{C}$ . Likewise, a comparable range of pore sizes can be achieved by flowing air saturated in toluene at  $20\text{ }^\circ\text{C}$  across the sample and heating the film between  $20\text{ }^\circ\text{C}$  and  $125\text{ }^\circ\text{C}$ .

toluene-saturated vapor also at  $20\text{ }^\circ\text{C}$ . Likewise, the dotted line (reading from the lower horizontal axis) depicts the  $r_c$  variations by heating the sample in the presence of a stream of air that has been saturated with toluene at  $20\text{ }^\circ\text{C}$ . In the simple model of the Kelvin equation, it should be possible to compare the non-isothermal physisorption data with the isothermal data. This requires first accounting for the temperature dependence in the non-isothermal data. This is simply done by equating  $r_c$  and accounting for the  $T$  dependence of  $\gamma$  and  $V_m$ :

$$\left(\frac{P}{P_0}\right)_{20^\circ\text{C}} = \left(\frac{P}{P_0}\right)_T \left(\frac{\gamma_{20^\circ\text{C}} V_{m,20^\circ\text{C}} T}{\gamma_T V_T 293}\right) \quad (6)$$

By correcting the  $T$  variation physisorption data this way, it should be possible to compare directly with isothermal physisorption data obtained with the  $P$  variation method. We elaborate on this later, ultimately



demonstrating that the two techniques are not equivalent; the simple Kelvin equation neglects thermal changes in the energy or heat of adsorption.

### 2.B.3. Pure Solvent Vapor

Thus far, the methods of controlling the partial pressure require using a carrier gas. However, it is possible to construct an environmental control system that utilizes pure solvent vapors. This may be advantageous in instances where the presence of the carrier gas affects the adsorption. Figure 10b schematically depicts how to construct a carrier gas-free environmental control system. In this case, the solvent reservoir is a 500 cm<sup>3</sup> stainless steel cylinder with two threaded ports (available from Swagelock). One of the ports is capped while the other is fitted with standard Swagelock fittings for 6.35 mm (1/4 inch) stainless steel tubing. Approximately 250 cm<sup>3</sup> of toluene is poured into the reservoir before connecting it to the pressure control valve (PCV). Our system used a MKS Instruments (Model 248A) pressure control valve with stainless steel valve seats. From the pressure control valve, flexible stainless steel vacuum tubing is used to connect to the ISO QF-25 flange on the sample chamber. A tee is added at this junction, and a MKS Instruments 626A 13TDE capacitance manometer is attached to read the absolute pressure of the sample chamber. Both the PCV and the capacitance manometer are connected to the MKS Instruments 146C control unit. The exit ISO QF-25 flange on the sample chamber is connected to an oil-free vacuum pump through the Kinetics Thermal System VT890A cold trap. An adjustable bleed valve is inserted into the vacuum line between the sample chamber and the vapor trap. There are also mechanical shut-off valves conveniently placed between each of the components, as indicated in Figure 10b.

The operating principle for this system is simple. After loading the toluene and sealing the Swagelock fittings, a dewar of liquid nitrogen is used to freeze the toluene in the solvent reservoir. The entire system is then evacuated to remove the air. Valve V<sub>1</sub> is then closed while the frozen toluene is allowed to thaw. We recommend repeating this freeze-thaw cycle a few more times to degas the toluene. Once the toluene is sufficiently degassed, valve V<sub>1</sub> is closed, and the entire system is evacuated one final time. The vacuum pump is left on and the bleed valve is partially closed to keep a modest pumping rate on the sample chamber. Then a pressure set point is entered into the 146C. When manual shut-off valve V<sub>1</sub> is opened, toluene vapor enters the sample



chamber, regulated by the PCV. We recommend gently warming the toluene reservoir (to approximately 50 °C) to generate a slight pressure difference; this temperature is chosen based on the temperature dependence of the toluene equilibrium vapor pressure and the minimum pressure difference across the valve specified by the manufacturer for good control. Since the vapor in the sample chamber is pure toluene, the partial pressure is read directly off of the capacitance manometer.

While this principle is simple, accurate pressure control with this system is difficult. We recently designed and built this system because of the attractive option of no carrier gases. However, unlike the previous methods, this system has an active control loop. As with any dynamic system, establishing the proper proportional, integral, and derivative gains to achieve stable control can be a challenge. This added level of complexity should be considered when choosing a method of environmental control. An alternative would be to use a quasi-static mode of operation that does not require closed loop control. With the vacuum pump on and the bleed valve properly set, the PCV could be *manually* opened by incremental amounts. For each setting of the PCV, a new equilibrium will be established by the balance of the toluene input and output flow rates. In each case, the equilibrated partial pressure would simply be read off of the manometer.

## 2.B.4. Choice of Adsorbate

In the preceding discussions, toluene is used as the organic vapor. However, the toluene can be replaced by any number of organic solvents or adsorbates. Gurvich's rule<sup>[23]</sup> states that the pore volume equals the volume of the adsorbed/condensed liquid at saturation, assuming that the molar volume of the adsorbate is the same as pure liquid at the temperature of interest. In this respect, the total porosity should not depend upon the solvent choice. This principle has been generally demonstrated in a wide range of mesoporous solids and adsorbates,<sup>[7]</sup> including a few low- $\kappa$  dielectric films studied by the EP technique.<sup>[3a]</sup> However, deviations from Gurvich's rule should be an important concern, especially in microporous solids where the pore size approaches the size of the adsorbate molecules. Geometric size restriction, steric limitations imposed by directional interactions with the walls and/or other molecules, or changes in the fundamental properties of the fluid/condensate can become appreciable. There is a large body of literature dedicated to understanding how fluids confined in nanopores change their fundamental properties (*e.g.*, see

references 24–43). For example, neutron diffraction measurements of the radial distribution function of benzene condensed in pores with diameters from 24 Å to 65 Å show that excluded volume effects increase as the pore size decreases.<sup>[27]</sup> This leads to a decrease of the fluid density in the nanopore as compared to bulk, suppression of the melting temperatures, and possibly even inhibited crystallization of the adsorbate.<sup>[28]</sup> One must also be aware that the different adsorbates display different affinities for the porous matrix material. We have seen fluorinated low- $k$  dielectric films where toluene would not wet the wall material and, therefore, experienced problems infusing the film with adsorbate. However, strong interactions with the wall material might induce swelling, or restructuring of the pore network. There are many factors that should be considered when choosing an adsorbate vapor. Toluene was selected here because: (1) the temperature dependence of the vapor pressure is appropriate to probe a reasonable range of pore sizes; (2) the low polarity liquid wets most (except the fluorinated example cited above) low- $k$  materials; and (3) most low- $k$  materials do not swell appreciably in the presence of toluene.

### 3. DATA REDUCTION AND ANALYSIS

#### 3.A. Reducing the X-ray Reflectivity Data

The raw reflectivity data taken directly from the instrument is reduced to a normalized reflectance defined as the ratio of the measured intensity at a given angle to the intensity of the direct beam ( $I/I_0$ ). In addition, the specular angle,  $\theta$ , should be reduced to  $Q$  through  $Q = (4\pi/\lambda)\sin\theta$ . These normalizations allow the data to be interpreted independent of the X-ray wavelength and/or varying X-ray beam intensities. Typically, the data are plotted as the logarithm of the reflectivity as a function of  $Q$  because the relative peak intensities of the Kiessig fringes decay very rapidly, as shown in earlier sections. There are two main considerations needed to properly normalize a reflectivity curve. First, one needs to correct for variations in  $I_0$  due to varying illumination areas that arise from the height of the X-ray beam at these shallow grazing incidence angles (the footprint effect). Second, the background intensity needs to be subtracted in order to ensure correct reflectivity values. Figure 9 shows the raw intensity data from an aligned sample in an X-ray reflectometer. The data in the low  $Q$  region before the critical angle show increasing reflected intensity with increasing angle. The finite height of the beam leads to an illuminated area at low specular angles that is often much larger than the sample size. Given the beam height, simple geometric formulas are sufficient to describe the relative area of illumination (assuming the sample is perfectly flat). For example, for a beam height of 0.5 mm (using the full width at half maximum from the derivative of a direct beam scan shown in Figure 8b), a beam width of 1 mm, and an incident angle  $\theta = 0.1^\circ$ , the area of illumination at the sample surface is approximately 286.5 mm<sup>2</sup>. Changes in this illumination area with increasing angle are well approximated with a linear function because the geometric formula is a sine function at very small angles. Therefore, the process for calculating  $I_0$  as a function of  $\theta$  is straightforward as follows:

1. Perform a linear fit to the footprint region of the X-ray reflectivity data before the first critical angle.
2. Calculate the  $\theta$  where the beam footprint area reaches the size of the sample.
3.  $I_0$  increases linearly with  $\theta$  up to this angle, then remains constant for larger  $\theta$ .
4. Normalize the measured X-ray intensity by the complementary  $I_0$  value.

For many X-ray reflectivity systems, the maximum of  $I_0$  can be taken to be the intensity value at the first critical angle. Nevertheless, it is recommended that all instrumental parameters be identified so that any sample size considerations can be coded into the data reduction software.

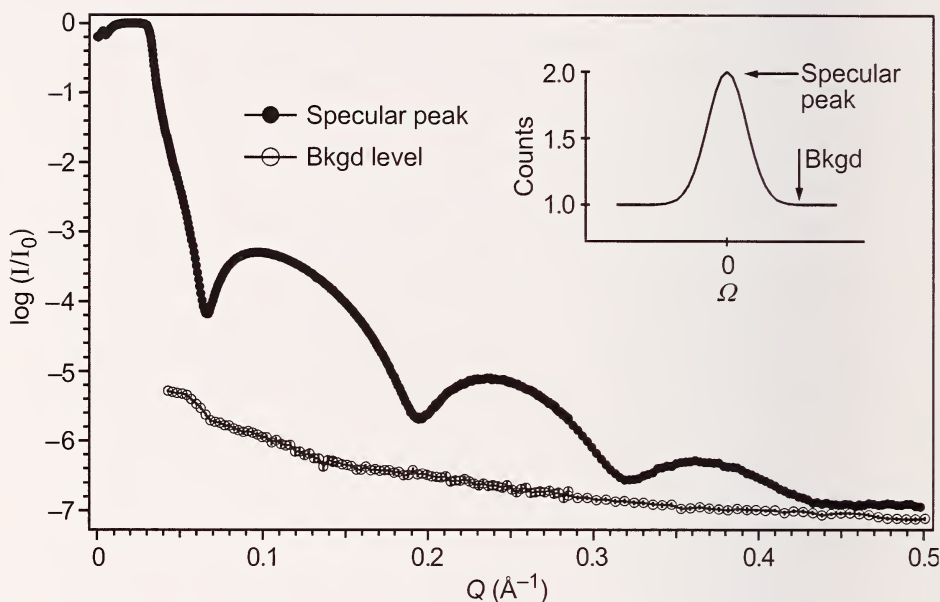


**Figure 13.** X-ray reflectivity data from a well-aligned sample and the intensity from the background as measured at an angle offset from the specular angle. The background level is indicated in the inset schematic. Standard uncertainties are smaller than the size of the data markers.

The second correction needed to properly reduce the X-ray reflectivity data is the subtraction of any background intensity that may arise from incoherent scattering or other instrumental effects (detector noise). If a sample is assumed to be flat (no lateral correlations), then the baseline from an off-specular rocking curve described earlier (*i.e.*, Figure 8e over a larger range — see inset of Figure 13) provides a good measure of the background intensity. Figure 13 shows both the specular X-ray reflectivity data ( $\Omega = 0$ ) and the background level collected by repeating the reflectivity measurement with  $\Omega$  sufficiently off-set so that the intensities are in the flat background region indicated in the inset. For X-rays, the background intensities from absorption and incoherent scattering are mostly negligible relative to the specular peak. Nevertheless, the background intensity should be evaluated to ensure



that this assumption is reasonable for the particular system and sample being used. It is also important to perform the background subtraction *before* normalizing the intensities with  $I_0$ .

### 3.B. Fitting the X-ray Reflectivity Data

A complete analysis of X-ray reflectivity data requires modeling the reduced data using well-established models and procedures. The equations needed to model specular reflectivity data are straightforward and known for many years.<sup>[14–19]</sup> The basic procedure involves constructing a model electron density depth profile consistent with well-known scattering length density parameters for the material or materials of interest, discretizing the model profile into material slices defined by their thickness and electron density, solving a recursion formula for the expected X-ray reflectivity data, then iterating the model profile until a satisfactory fit is obtained with the experimental reflectivity curve. The biggest limitation in the analysis of X-ray reflectivity data is the need for a model profile to fit to the data. Direct inversion of the reflectivity data to obtain the electron density profile is not possible because one measures the intensity of the reflected beam but not the phase of this reflection (the inverse problem). There are many different software packages available to fit X-ray reflectivity data, and it is beyond the scope of this practice guide to evaluate the options. References [17–19] provide a good review of the existing literature on this active field of research.

For XRP, it is often sufficient to measure just the critical angle of the sample because changes in the amount of adsorption are proportional to the changes in the sample electron density. For more detailed analysis, it may become necessary to perform full data fits of the XRP reflectivity curves for situations: for example, where the film swells, if the pore size distribution is not uniform through the film, or if the initial film itself is not uniform. The following sections show how the X-ray reflectivity data can be used to determine important information about the structure of nanoporous, thin films.

### 3.C. Interpretation of XRP Data

In this section, we illustrate how to interpret and analyze XRP by way of example, focusing on films from three different classes of porous low- $k$  dielectric material. The films will be characterized in terms of critical structural information, such as the average film density, average wall material density, porosity, and the pore size distribution. By way of introduction, the first class of material is a hydrogensilsesquioxane (HSQ) film prepared by the evaporation of a high boiling point solvent after



gelling the HSQ resin.<sup>[4a]</sup> The second is a methylsilsesquioxane (MSQ) film generated through a templated vitrification of low-molecular mass, siloxane oligomers.<sup>[44]</sup> The third material is deposited by plasma enhanced chemical vapor deposition (PECVD) from a mixture of an organic precursor (the porogen) and tetramethylcyclotetrasiloxane.<sup>[45]</sup> This last film will be referred to as porous SiCOH. The reported dielectric constants of the porous HSQ, MSQ, and SiCOH films are 2.20, 1.85 and 2.05, respectively. In light of the nominally similar dielectric constants, we contrast the detailed pore structures in these films since the latter also affect critical aspects like the mechanical properties of the film. The ensuing discussion effectively demonstrates how XRP is able to perceive subtle differences in the pore structures of these otherwise similar low- $k$  films. Later, the characteristics of the porous films obtained from XRP are compared with similar data obtained through scattering, specifically the SANS/SXR techniques described elsewhere.<sup>[4]</sup>

Figure 14 displays experimental SXR data for the three porous low- $k$  films both under vacuum and in the presence of toluene-saturated air. The data are presented as the logarithm of the reflectivity ( $I/I_0$ ) as a function of  $Q$ . As the incident angle (*i.e.*,  $Q$ ) increases, the X-rays first penetrate the film at the critical wave vector  $Q_c$ , at which point the

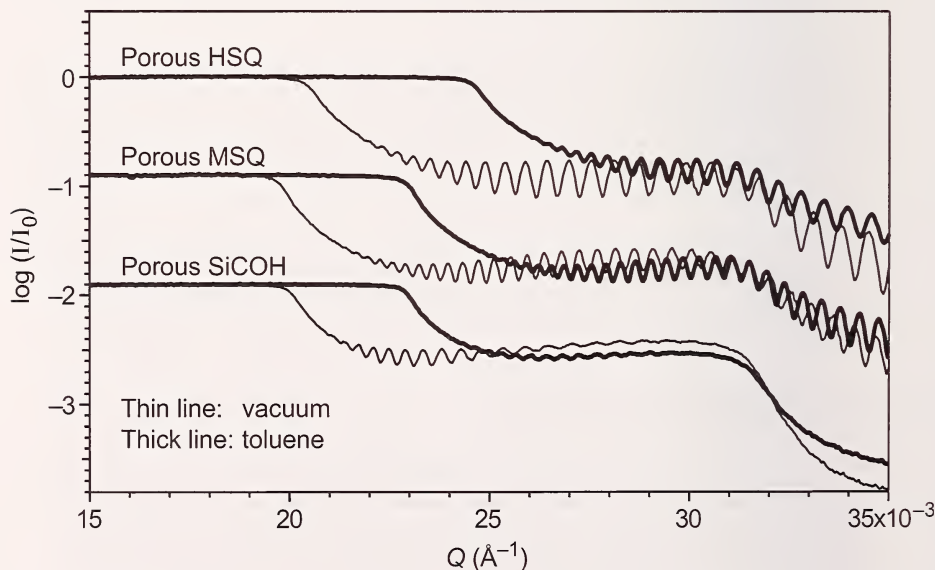


**Figure 14.** SXR curves of porous HSQ, porous MSQ, and porous SiCOH thin films. The curves are offset for clarity. The standard uncertainty in  $\log(I/I_0)$  is less than the line width.

reflectivity drops sharply. The square of this critical angle is proportional to average electron density of the film, as discussed with Eqs. (4) and (5), which is then used to calculate the average mass density from the atomic composition. The atomic composition of these films is determined experimentally via ion beam scattering, using the combination of the Rutherford backscattering, forward scattering, and forward recoil scattering techniques discussed elsewhere.<sup>[4a,20]</sup>

Comparing the reflectivity curves under vacuum in Figure 14 shows that  $Q_c$  occurs at lower  $Q$  for the films with lower  $k$ , qualitatively indicating that the density of porous thin film decreases with the dielectric constant. It is also clear that  $Q_c$  shifts to higher  $Q$  in the presence of the saturated toluene vapor. Capillary condensation of the toluene inside the accessible pores results in an appreciable increase of the density. A larger difference between  $Q_c$  of the vacuum and the toluene-saturated curves indicates a greater uptake of toluene, and thus a greater porosity. From these two curves alone, one can calculate the total amount of toluene adsorbed, thus the total porosity  $P$ , as well as the density of the wall material  $\rho_{wall}$  separating the pores.<sup>[46]</sup> A simple rule of mixtures leads to two equations and two unknowns:

$$\rho_{dry} = (1-P)\rho_{wall} \quad (7)$$

$$\rho_{sat} = P\rho_{liquid} + (1-P)\rho_{wall} \quad (8)$$

In addition to  $P$  and  $\rho_{wall}$ ,  $\rho_{dry}$  is the total average density of the dry (evacuated) film,  $\rho_{sat}$  is the average density of the film in the presence of the saturated vapor, and  $\rho_{liquid}$  is the density of the condensed liquid.  $\rho_{dry}$  and  $\rho_{sat}$  are defined by the  $Q_c^2$  values of the reflectivity experiments in the dry and vapor-saturated environments, respectively, while  $\rho_{liquid}$  is assumed to be bulk-like. To convert the  $Q_c^2$  values into  $\rho_{dry}$  and  $\rho_{sat}$ , use the elemental composition of the low- $k$  film, the elemental composition of the toluene condensate, and Eqs. (3) and (4) to convert the electron densities into mass densities. Knowing  $\rho_{dry}$  and  $\rho_{sat}$  leaves two equations that can be simultaneously solved for the remaining two unknowns,  $P$  and  $\rho_{wall}$ .

Eqs. (7) and (8) do not account for pores that may be inaccessible to the condensing vapor; such porosity is folded into the average wall density of the material. Pores might not be accessible if they are isolated, not interconnected to the surface, too small to accommodate the vapor molecules, or excluded because of an unfavorable surface energy.

Our experience with a broad range of low- $k$  dielectric materials indicates that toluene is able to access most pores; toluene has low polarity and wets most low- $k$  materials, which by their nature must be engineered with low polarity (*i.e.*, polar groups lead to higher dielectric constants, and these are designed to be low- $k$  films). The only exception, however, was the highly fluorinated materials that the toluene did not wet or penetrate the wall material.

Eqs. (7) and (8) also do not account for swelling of the low- $k$  film by the condensate. XRP is, however, well suited to address swelling because X-ray reflectivity provides a highly accurate measure of film thickness. Using toluene vapor, we rarely see evidence of film swelling greater than 1 % in thickness for most non-organic low- $k$  materials. Sometimes polymeric films will swell appreciably in the presence of toluene, but for most low- $k$  materials this is not the case. In some respects, a small amount of film swelling may in fact be desirable. If the condensate can gently swell the film, without altering the pore structure, it is reasonable to assume that all the pores are accessible. Swelling means that the condensate diffuses through the wall material, ensuring that all pores are accessible. In the presence of swelling, Eq. (8) should be modified such that the porosity is given by:

$$P = \frac{\rho_{sat}t_{sat} - \rho_{dry}t_{dry}}{\rho_{liquid}t_{dry}} - \frac{t_{sat} - t_{dry}}{t_{dry}} \quad (9)$$

where  $t_{dry}$  and  $t_{sat}$  are the film thickness values of the dry and swollen films. This equation assumes that the volume of liquid toluene is conserved (rule of mixtures) upon absorption into the film and the wall material. Once  $P$  is determined, Eq. (7) can be used to extract  $\rho_{wall}$  for the dry material.

The porosities obtained by this method (no swelling, Eqs. (7) and (8)) for the porous HSQ, MSQ, and SiCOH films are  $(46 \pm 1) \%$ ,  $(34 \pm 1) \%$ , and  $(31 \pm 1) \%$ , respectively. The resulting wall densities of the porous HSQ, MSQ, and SiCOH films are  $(1.83 \pm .05) \text{ g/cm}^3$ ,  $(1.35 \pm .05) \text{ g/cm}^3$  and  $(1.31 \pm .05) \text{ g/cm}^3$ , respectively. Notice that the porous HSQ film has the highest porosity, yet its dielectric constant is the largest. This apparent contradiction is understood through the observation that the porous HSQ film also has the highest wall density. It is also interesting that the porous MSQ and SiCOH films have similar average densities, wall densities, and atomic compositions, despite the fact they are prepared from very different techniques. The elemental composition, detailed

**Table 1.** A summary of the atomic compositions, dielectric constants ( $k$ ), and structural characteristics of different porous low- $k$  films. The estimated standard uncertainties of the atomic compositions,  $Q_c^2$ , densities, porosities and pore radii are  $\pm 2\%$ ,  $0.05 \text{ \AA}^{-2}$ ,  $0.05 \text{ g/cm}^3$ ,  $1\%$ , and  $1 \text{ \AA}$ , respectively.

Porous Film	Atomic Composition (Si:O:C:H)	$k$	$Q_c^2$ ( $\times 10^{-4} \text{ \AA}^{-1}$ )	$\rho_{dry}$ ( $\text{g/cm}^3$ )	$\rho_{wall}$ ( $\text{g/cm}^3$ )	P (%)	Pore Radius ( $\text{\AA}$ )	
							XRP	SANS
HSQ	25:48:7:20	2.20	4.25	0.98	1.83	46	13	9
MSQ	15:25:19:41	1.85	3.95	0.89	1.35	34	15	10
SiCOH	10:20:28:42	2.05	4.04	0.91	1.31	31	5	3

structural characteristics, and standard uncertainties in the pore characteristics of the samples are summarized in Table 1.

The sensitivity and resolution of SXR are sufficient to reveal subtle differences between the three films as the toluene gradually infiltrates the pores as the partial pressure varies from  $P/P_0 = 0$  (pure air) to  $P/P_0 = 1$  (toluene saturated). In terms of the reflectivity data, Figure 15 illustrates

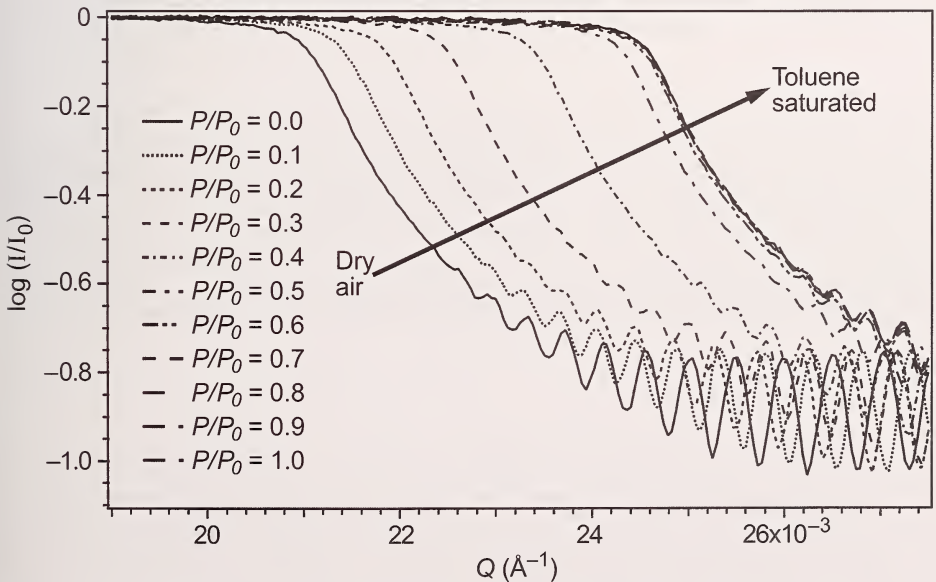


**Figure 15.** Critical angle changes for the porous HSQ sample as  $P/P_0$  increases systematically from 0 (dry air) to 1 (toluene-saturated air). Condensation of the toluene inside the pores results in an appreciable and measurable change in  $Q_c^2$ .



these changes in the porous HSQ film in the region of  $Q_c$ . By assuming that the mass density of adsorbed toluene is the same as that of the bulk fluid, the increase in  $Q_c^2$  above the vacuum level can be used to calculate the amount of toluene adsorbed into the film as a function of the relative partial pressure. These data are presented as physisorption isotherms in Figure 16, completely analogous to the examples discussed in Figure 1.

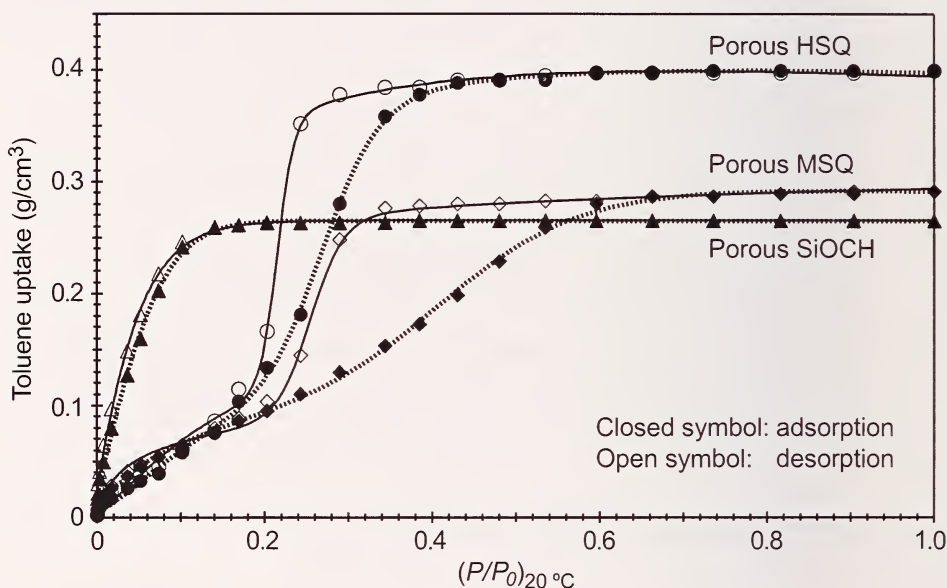


**Figure 16.** Physisorption isotherms for the porous HSQ, MSQ, and SiCOH films. The lines are smooth fits using the cumulative sum of a sigmoidal and a log-normal function for porous HSQ and MSQ films, and the sum of a Gaussian and a sigmoidal function for porous SiCOH film. We generally recommend fitting these physisorption isotherms with such arbitrary fit functions. If the curve faithfully parameterizes the experimental data, it will be helpful later in extracting a smooth pore size distribution (discussed later in Figure 18). Estimated standard uncertainties are comparable to the size of the data markers.

In Figure 16 for the porous SiCOH film, there is a prominent uptake at low partial pressures that quickly levels off. There is also no hysteresis between the adsorption and desorption branches. This is characteristic of filling micropores (pores less than 2 nm in diameter),<sup>[7–9,12]</sup> indicating that the PECVD process generates a large population of small pores. In comparison, the porous MSQ film continues to adsorb over a broad range of larger partial pressures. There is also a pronounced hysteresis between the adsorption and desorption pathways for the porous MSQ



film, consistent with the filling of larger mesopores.<sup>[7–9,12]</sup> This indicates that the porogen in the PECVD film forms smaller domains than the spin-cast MSQ film, leading to smaller pores in the porous SiCOH film. This is striking because the porous SiCOH and MSQ films are otherwise similar in terms of their atomic composition, total porosity, and wall densities; the primary difference is in their pore size distributions (PSDs). At low partial pressures, the adsorption process in both spin-on-glass (SOG) films (porous HSQ and MSQ films) is gradual at first, but it increases steeply at intermediate partial pressures due to capillary condensation in the mesopores. After these mesopores are filled, the adsorption isotherms level off. Note that capillary condensation and evaporation do not take place at the same partial pressures, *i.e.*, there is an appreciable hysteresis. The hysteresis loop in the MSQ film is highly asymmetric (broad on adsorption, narrow on desorption), suggesting that pore connectivity (network) effects are important.<sup>[47]</sup> If larger pores can only be accessed through neighboring or interconnected narrow pores, the larger pores are not free to desorb at the relative pressure corresponding to their critical capillary radius. The smaller pores block the desorption of the larger pores in a manner that has been described as the “ink-bottle” effect in the porosimetry literature.<sup>[7,48]</sup> The result is a simultaneous draining of both the small- and large-mesopores at a partial pressure corresponding to the critical radius of the smaller pores. Hence the sharper drop in the desorption curve as compared to the adsorption branch in Figure 16.

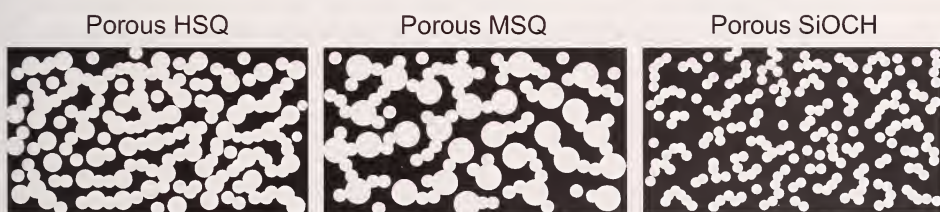


**Figure 17.** Schematic pore structures for the porous HSQ, MSQ, and SiCOH films.

By comparing the general shape of the adsorption/desorption isotherms for the three different films, one can qualitatively arrive at the schematic pore structures depicted in Figure 17. The PECVD process creates small pores in very large quantities. The lack of a hysteresis loop confirms that the dimensions of pores are on the order of a few toluene molecules. These pores, as well as all the films studied here, are apparently interconnected since toluene freely diffuses into and out of

the structures. The total porosity is, however, greater in the HSQ material as indicated by the largest total toluene uptake in Figure 16. The pores in the porous HSQ are also clearly larger than the PECVD material's pores. Like the pores in porous SiCOH, those in the porous HSQ are fairly uniform in their size distribution as indicated by the symmetric and relatively narrow hysteresis loop. This is in contrast to the MSQ film with its very broad pore size distribution and the largest average pore size (despite the lower porosity in comparison to the HSQ film). As discussed above, the sharp desorption branch of the MSQ film in contrast to the broad adsorption pathway indicates that pore blocking effects are significant.

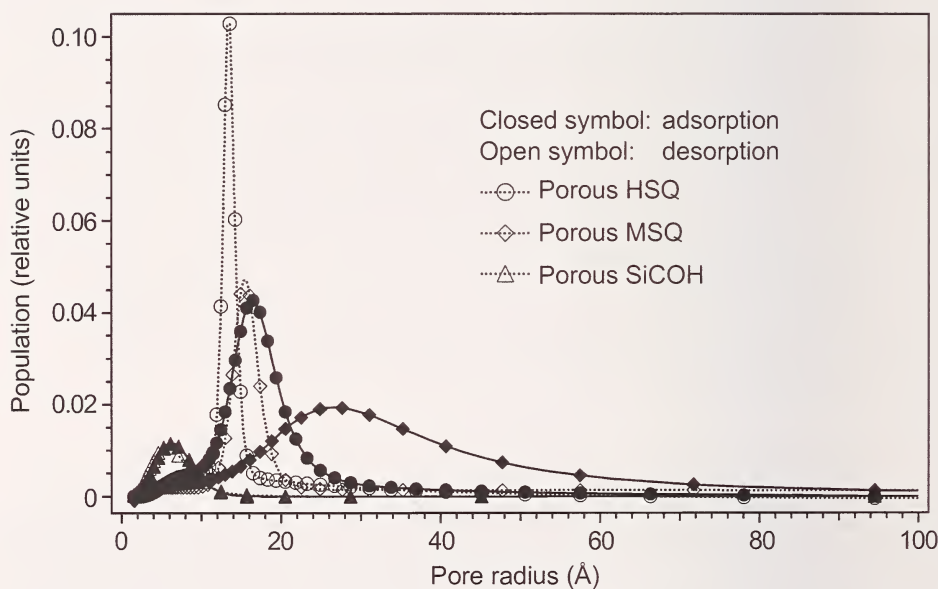


**Figure 18.** Approximate pore size distributions from the fits (not data) through the physisorption isotherms in Figure 16, using Eq. (1) used to convert  $P/P_0$  into a pore size. The distributions from the adsorption branch (solid lines) can be significantly broader and shifted to larger pore sizes than the corresponding desorption branch, especially in those materials (like the MSQ film) with a large distribution of mesopore sizes.

This qualitative description can be quantified using Eq. (1) to convert the partial pressures for capillary condensation in Figure 16 into pore radii. Plotting the relative toluene uptake as a function of the pore size establishes the pore size distribution (PSD). To illustrate this procedure, we use the simplest example of the Kelvin equation (Eq. (1)) to convert

$P/P_0$  into a critical radius for capillary condensation. However, we acknowledge that alternative expressions to Eq. (1) may be more appropriate. The Kelvin equation lacks terms that account for interactions of the condensate with the pore surfaces and is not particularly well suited for situations where the pore size approaches the dimensions of the condensate molecule; these items are discussed in greater detail in the Special Concerns section below. Nevertheless, Figure 18 shows the resulting pore size distribution, with the total areas beneath the curve scaled to a value consistent with the total  $P$  for each film as reported in Table 1. It should be noted that the symbols in Figure 18 do not represent actual data; they are generated from the smooth fits described in the caption of Figure 16. Generally, we find that the increments of  $P/P_0$  in experimental data of Figure 16 are not sufficiently fine for a point-by-point differentiation when using a Kelvin equation to generate Figure 18; significantly smoother and reasonable distributions are obtained by transforming the arbitrary fit function. As long as the empirical fit accurately parameterizes the physisorption data, this is a reasonable procedure.

In the porosimetry literature, it is traditional to use the desorption branch of the physisorption isotherms to report the PSDs. The average pore radii in the porous HSQ, MSQ, and SiCOH films taken from the desorption curves in Figure 18 are approximately 13 Å, 15 Å, and 5 Å, respectively. However, it is important to realize that this average is biased towards the minimum or constricting pore in regards to the ink-bottle effect; a more complete interpretation of the pore structure always results from analyzing both the adsorption and desorption branches. For example, in Figure 18 notice that there is a relatively large difference between adsorption and desorption pore size distributions for the MSQ materials. While the average pore radius on desorption was approximately 15 Å, the desorption branch leads to an approximate average pore radius of 27 Å. By contrast, the discrepancy is much less for the HSQ film (ca. 13 Å on desorption and 16 Å on absorption) and nearly the same (no discrepancy) for the SiCOH film. This is consistent with the previous discussion of the isotherms in Figure 16 and the schematic pore structures in Figure 17.

Small angle neutron scattering (SANS) is also capable of quantifying the average pore size in these low- $k$  dielectric films, providing a basis for comparing for the XRP data. The SANS measurements discussed herein are done on the NG1 beam line at the National Institute of Standards and Technology Center for Neutron Research. The SANS data are collected with the sample under vacuum, like the XRP, and shown in Figure 19.

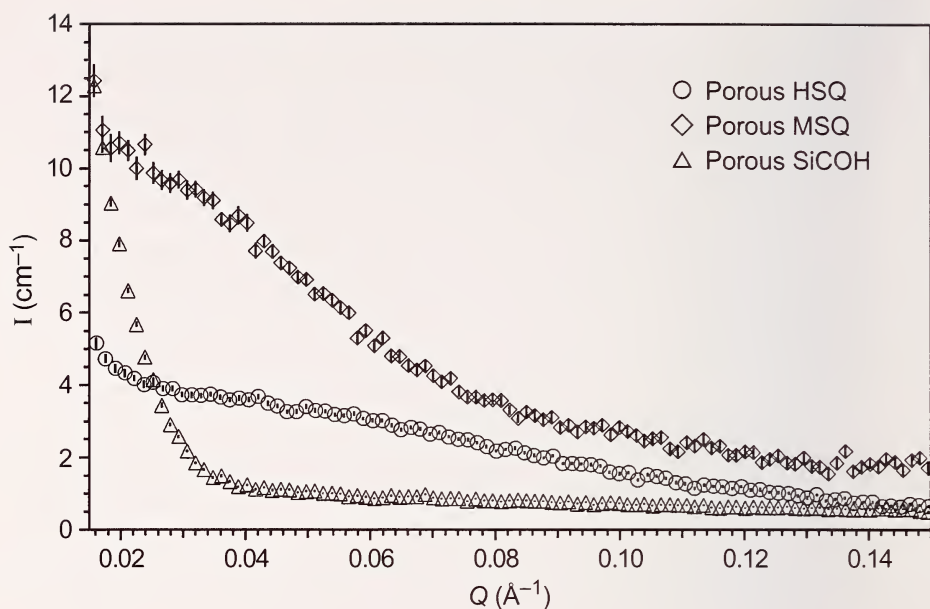


**Figure 19.** SANS data for the porous HSQ (circles), MSQ (diamonds), and SiCOH (triangles) films under vacuum. Error bars, usually smaller than the data markers, indicate the standard uncertainty in the absolute intensity.

These scattering curves can be fit with the Debye model<sup>[49]</sup> to extract an average pore size. A detailed discussion of the SANS data is beyond the scope of this guide. Briefly, an increase in the scattering intensity corresponds to increase in the pore size and/or porosity. In Figure 19 the porous SiCOH film shows noticeably weaker scattering than either of the porous SOG films, which is consistent with the smaller pore size and lower porosity. The greatest scattering intensities occur in the porous MSQ film, which is also consistent with the greatest population of larger pores. For the porous HSQ and MSQ films, the Debye model gives reliable fits with average pore radii of 9 Å and 10 Å, respectively. The radii are comparable to the XRP pore sizes reported in Table 1. Unfortunately, the SANS intensities in the porous SiCOH film are too low to reliably apply the Debye model; the scattering is not strong from this low porosity film. If the Debye model were applied, the resulting pore radius would be approximately 3 Å. This result is unphysical in light of the implicit assumption in the Debye model that there is a distinct interface between the pore and the wall material; 3 Å is comparable to a single atomic radius, meaning that the model is inappropriate. Nevertheless, there is reasonably good agreement between the SANS and XRP data for



the higher porosity HSQ and MSQ films. We must also mention that there are examples, not reported here, of where the SANS and XRP data do not yield consistent data. The agreement, or lack of agreement, between the XRP and SANS data here is not of particular significance. Recall the discussion above of the oversimplifications of the Kelvin equation; this was chosen as the simplest case example for demonstration. Likewise, SANS also suffers from the “inverse problem” in that pore sizes can not be obtained directly from inversion of the scattering data; a model (here the Debye model was used) must be invoked. To a large extent, the agreement between SANS and XRP will depend on the consistency of the models chosen to analyze the pore size distributions.

More relevant than the quantitative agreement between the SANS and XRP, it is important to realize that XRP is a highly sensitive porosimetry, well suited for materials with very small pores. This is illustrated with the porous SiCOH film. SANS is unable to perceive the porosity in this film because pores are too small, below the resolution limit of the technique. However, in Figure 14 there is still a very significant change in the raw XRP data as toluene condenses inside the pores. Because of this extraordinary sensitivity, XRP is superior to SANS or other scattering techniques for thin films with very small pores.

One distinct advantage of XRP over other forms of porosimetry, including the sister ellipsometric porosimetry technique,<sup>[3]</sup> is the potential to vertically depth profile the density (and therefore porosity) through the thickness of the film. Recall that the reflectivity data is fit using a multi-layer model. In the preceding examples, the low- $k$  films were modeled with a single layer of uniform density, both under vacuum and in the presence of toluene. However, Figure 20 shows an example of a low- $k$  dielectric film that has a multi-layer structure with different porosities in the different layers. Figure 20a shows the reflectivity data for this film both under vacuum and in the toluene-saturated environment. Notice that the general shape of the reflectivity curves is noticeably different from the preceding examples. In addition to the high-frequency interference fringes reflecting the total film thickness, there are also lower frequency oscillations in the data as roughly indicated by the lines and arrows; a fourier transform of this data would reveal multiple characteristic frequencies. The low frequency oscillations stem from the multi-layer nature of the structure. Fitting this reflectivity data requires 3 distinct layers for the low- $k$  film, as revealed in Figure 20b. Here the electron density of the layers as a function of distance into the film (starting from the free surface) is plotted in terms of  $Q_c^2$ . Near the free surface (layer 1) the density is noticeably larger than the



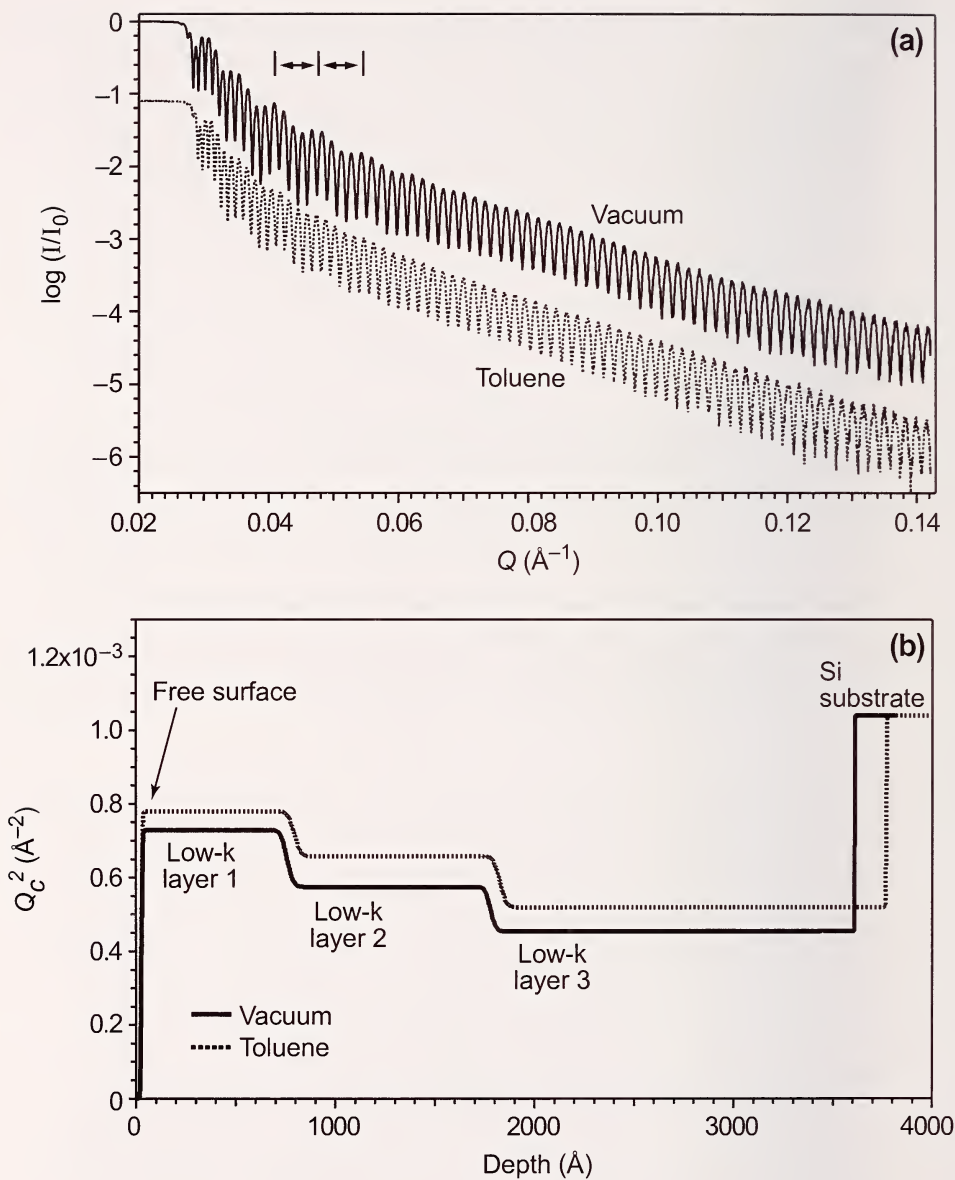


**Figure 20.** XRP data for a low-k film comprised of 3 distinct layers. Part (a) shows the reflectivity data for the dry and toluene-saturated films, revealing both a high-frequency periodicity due to the total film thickness and low-frequency oscillations due to the thinner individual layers. Part (b) shows the real space scattering length density profiles as a function of distance into the film, revealing the thickness and density of the individual layers.

rest of the low- $k$  film, the consequence of a plasma treatment to the surface. Also note that the density appears lowest (layer 3) near the Si substrate.

When this multi-layer film is exposed to the toluene environment, two effects become immediately obvious. First, the density increases in all three layers as toluene condenses in the individual pores. Second, the total film thickness swells by approximately 4.4 %, meaning that Eq. (9), not (8), must be used to extract the porosities. What may be less obvious is that each of the 3 layers picks up different amounts of toluene. Qualitatively, Figure 20b shows that layer 2 takes in the most toluene while layer 1 picks up the least. Quantitatively, we can use Eq. (9) to predict that the porosities in layers 1, 2, and 3 of this low- $k$  film are approximately 13 %, 21 %, and 16 %, respectively. Despite the lower overall electron density in layer 3, the greatest porosity is found in layer 2. This is because the wall densities are also greater in layer 2, offsetting the porosity effect in terms of the average film density. This example demonstrates the power of XRP in extracting depth-dependent, detailed pore information.

### 3.D. Special Concerns

#### 3.D.1. Quantitative Interpretation of the Physisorption Isotherms

The shapes of the adsorption/desorption isotherms in Figure 16 readily convey a wealth of qualitative information regarding the pore structure. However, it can be a challenge to quantify these characteristics in terms of both the average and distribution of pore sizes. This is equally true for the thin porous films presented here as well as all physisorption isotherms in general; this is not a specific limitation of X-ray porosimetry. The adsorption/desorption process is complex and affected by many factors. Consequently there are several ways to interpret the isotherms, each focusing on different aspects or based on different assumptions. Generally, these analysis schemes can be grouped into three general classes. The first group emphasizes the initial stages of adsorption, while the first monolayer(s) of adsorbate adhere to the surface. Well-known examples include the Henry's Law type analyses, the Hill-de Boer equation,<sup>[50]</sup> the Langmuir theory,<sup>[51]</sup> and the Brunauer-Emmett-Teller (BET) analysis.<sup>[52]</sup> These theories have been developed primarily for adsorption onto non-porous solids and are surface-area techniques.

The low partial pressure regions of an isotherm are also where micropore filling occurs. Micropores, with widths less than 2 nm, are easily filled by a few monolayers of most adsorbents, and the second group of equations or theories attempt to extract micropore characteristics from the initial stages of the isotherm. These are similar to the surface area techniques and include Henry's Law based interpretations, the Langmuir–Brunauer equation,<sup>[53]</sup> and the Dubinin–Stoeckli based theories.<sup>[54, 55]</sup> In systems that have very small pores, like the porous SiCOH film, these types of analysis are probably more appropriate than the Kelvin equation.

The final group of equations focuses on the latter stages of adsorption, where the mesopores (ca. 2 nm to 50 nm in width according to the IUPAC definition<sup>[7, 13]</sup>) are filled. This is the region where capillary condensation occurs, and the Kelvin equation is the simplest of these interpretations. There are numerous variations on the Kelvin equation that account for effects like multilayer adsorption prior to capillary condensation (*i.e.*, BJH method<sup>[56]</sup>), disjoining pressure effects in the condensed liquid (*i.e.*, DBdB method<sup>[57]</sup>), etc. However, it is not our intention to ascertain which adaptation of the Kelvin equation is most appropriate. This will vary significantly with the nature of the adsorbate and the porous material. Rather, we applied the simplest form of the Kelvin equation (see Eq (1)) to demonstrate the technique. These variations of the Kelvin equation are easy to implement, but the underlying assumptions should be carefully considered for each different experimental consideration. For assistance in evaluating which analysis method is most appropriate, we recommend the recent textbook by Rouquerol, *et al.*<sup>[7]</sup>

Eq. (1) provides the simplest possible Kelvin equation conversion between  $P/P_0$  and the pore sizes. Figure 18 displays the corresponding pore size distributions extracted from data in Figure 16. Notice that pore size distributions have been extracted from both the adsorption (solid lines) and desorption (dotted lines) branches of the isotherm, and that the distributions are always broader and shifted to a higher average pore size for the adsorption branch. This discrepancy is especially evident for the highly porous samples and consistent with the pore-blocking effects discussed earlier. It is sometimes a “general practice” in the porosimetry field to report pore size distributions for the desorption branch of the isotherm. However, in the presence of pore blocking this leads to artificially narrow and smaller distributions. It is crucial to look at both the adsorption and desorption isotherms to obtain a more comprehensive understanding of the pore structure. Once again,

though, this criticism is applicable to all forms of porosimetry and is not unique for X-ray porosimetry.

The pore size distributions in Figure 18 are approximate and only intended to demonstrate the technique. The average sizes are below 20 nm, which means that interpretations in terms of simple capillary condensation may be in error by well over 100 %.<sup>[58–60]</sup> Generally, the physics of capillary condensation in pores smaller than 20 nm is poorly understood. Studies show that more accurate interpretations require computer modeling and/or simulations of the isotherms. Gage Cell Monte-Carlo (GCMC) simulations and non-linear density functional theory (NLDFT) methods<sup>[58–60]</sup> have recently been developed to interpret adsorption/desorption isotherms from nanoporous materials and reveal that all of the existing interpretations of capillary condensation fail to extract reliable pore sizes. Currently, these GCMC and NLDFT techniques are the only reliable methods for understanding capillary condensation in pores significantly smaller than 20 nm and should, therefore, be considered when studying low- $\kappa$  dielectric films.

It is important to realize that this issue of the actual pore size is a matter of interpretation, but the raw isotherms in Figure 16 are robust. Likewise, the relative differences between the different materials are obvious and reliable. Porosimetry in general is very model dependent. To interpret the data one must assume a model and then verify how well it fits the data. This does not ensure that the solutions obtained are unique. To reach a proper interpretation requires supporting information, like the nature of the interactions between the adsorbent and adsorbate, feasible schemes for the pore architecture (*i.e.*, isolated spheres, interconnected channels, fractals), etc. This type of supporting data will help facilitate a correct interpretation of the isotherms.

### 3.D.2. Isothermal Control

In the experimental section, we discussed the different methods by which the  $P/P_0$  ratio can be varied, focusing specifically on the isothermal mixing of dry and toluene-saturated airstreams (the  $P$  variation method) as well as the controlled variation of the sample temperature in the presence of air saturated at 25 °C with toluene (the  $T$  variation method). With both of these techniques, accurate temperature control of the sample is imperative because  $P_0$  is very temperature sensitive; inaccurate physisorption isotherms will be obtained if the temperature control is poor. A clear illustration of this



is seen in Figure 21 below where several physisorption isotherms are shown for the same porous HSQ material discussed earlier. Examining the desorption pathways using the  $P$  variation technique, for which the sample temperature was maintained at  $25\text{ }^{\circ}\text{C}$ , the triangles correspond to a desorption curve where the control unit failed and the sample was maintained at  $(25 \pm 1.5)\text{ }^{\circ}\text{C}$ , while asterisks represent good thermal control of  $(25 \pm 0.1)\text{ }^{\circ}\text{C}$ . The two desorption pathways are different and would lead to large differences if the average pore size and distributions were calculated. The required accuracy of the temperature control will depend upon how temperature sensitive the vapor pressure is. For toluene we recommend the temperature be controlled to within a tenth of a degree for reproducible physisorption data.

### 3.D.3. Time Dependence of Desorption

In all of the physisorption isotherms presented thus far, approximately 30 min is allowed for equilibration after each  $P/P_0$  change, for both the

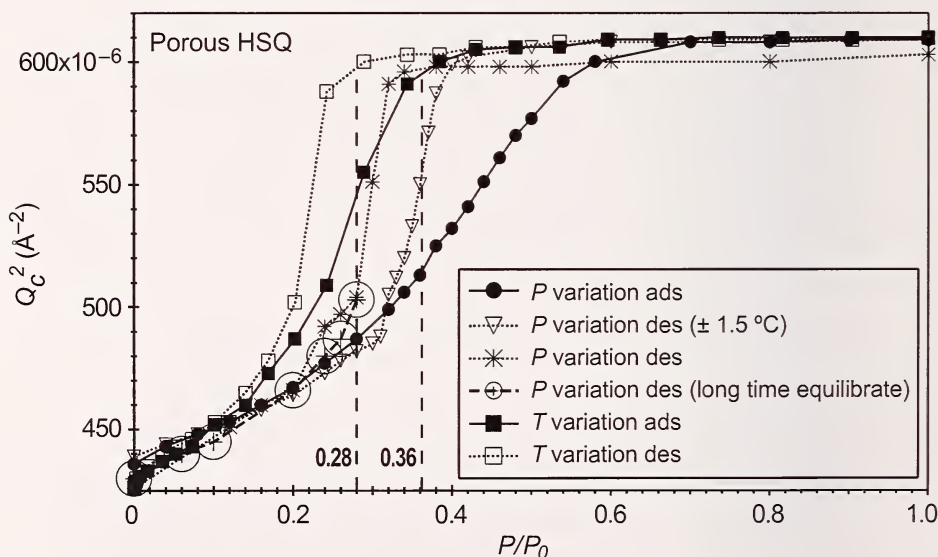


**Figure 21.** Physisorption isotherms generated by the T (squares) and P (all other data markers) variation methodologies of controlling  $P/P_0$ , as described in the text. The two techniques do not produce identical isotherms indicating that adsorption is not temperature invariant. Notice the discontinuous nature of the desorption pathways of the P variation technique. These discontinuities can be attributed to insufficient equilibration times, as described in the text and in reference to Figure 22. The estimated standard uncertainty in  $Q_c^2$  is comparable to the size of the data markers.



$T$  and  $P$  variations techniques. This is based on initial studies on the time dependence of the  $Q_c^2$  variations after a step increase of  $P/P_0$  from 0 to 1.0. We generally found that  $Q_c^2$  would continue to increase for approximately 15 min after such a step increase, finally reaching a time invariant plateau; 30 min equilibration times were deemed reasonable. This was further reinforced by the fact that the measurements paused at a given  $P/P_0$  in the adsorption branch and held over night would resume with the same  $Q_c^2$  value the next morning. However, eventually we noticed that measurements could not be paused reversibly in the region of steep descent on the desorption branch of the hysteresis loop;  $Q_c^2$  would continue to drop significantly in this region while  $P/P_0$  was held constant. This is shown in Figure 21. On the desorption branch with the open triangles, notice that the curve looks discontinuous in the region between the two dashed vertical lines at  $P/P_0 = 0.28$  and  $P/P_0 = 0.36$ . The location of this discontinuity coincides with a 12 h pause in the data collection. Likewise, a similar discontinuity is seen in the asterisks 3 points below the  $P/P_0 = 0.28$  vertical line. The desorption branch with the asterisk data markers starts turning concave up just below  $P/P_0 = 0.28$ , but then

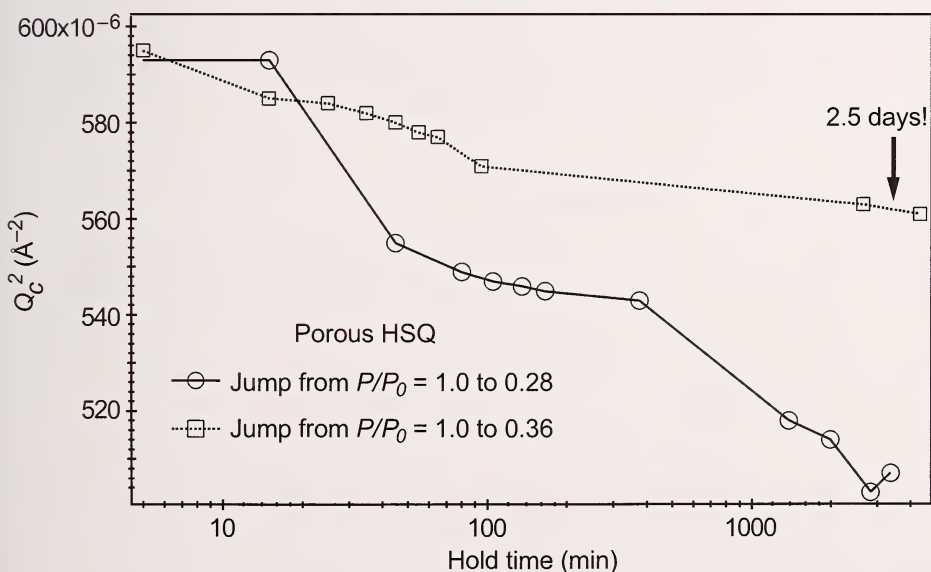


**Figure 22.** Time dependence of the  $Q_c^2$  variations in the porous HSQ sample after  $P/P_0$  jumps from 1.0 to 0.36 (squares) and 1.0 to 0.28 (circles). Notice that  $Q_c^2$  continues to evolve for several hours after the jump, indicating the equilibrium is difficult to achieve on the desorption branch. The same time dependence is curiously absent upon adsorption. The estimated standard uncertainty in  $Q_c^2$  is comparable to the size of the data markers.

a discontinuous jump occurs at  $P/P_0 = 0.20$ . This discontinuity also coincides with a pause in the data collection. When the desorption branch in this region is repeated, ensuring sufficient equilibration after each  $P/P_0$  change, the large open circles and heavy dotted line indicate the smooth equilibrium desorption path.

To explore the time dependence of the  $Q_c^2$  variations on adsorption/desorption further, we performed the following experiments. Using the  $P$  variation technique,  $P/P_0$  jumps from 1.0 to 0.28 and 1.0 to 0.36 were imposed onto the same porous HSQ displayed in Figure 21. The evolution of  $Q_c^2$  was then tracked over extended periods of time, as shown in Figure 22.  $Q_c^2$  decreases very slowly, reaching a plateau only after several days (note that in Figure 22 the time axis is logarithmic). Surprisingly, this time dependence is not observed if the sense of the  $P/P_0$  jump is reversed, *i.e.*, from 0 to 0.28 or 0.36; under these conditions equilibrium is rapidly achieved, consistent with the original 30 min equilibration times. The reason for these differences between the adsorption and desorption pathways is not understood. We suspect that it reflects diffusion of the toluene through the matrix walls at low partial pressure as opposed to adsorption. Regardless, this clearly means that equilibrium desorption isotherms may be difficult to achieve. Simple parameters like the rate of  $P/P_0$  change can affect the resulting pore size distributions. Care must be exercised, especially on the desorption pathways, to ensure that equilibration is achieved.

### 3.D.4. $P$ versus $T$ Variations of $P/P_0$

Figure 21 also displays physisorption isotherms corresponding to the  $P$  (circles — the equilibrium data) and  $T$  (squares) variation techniques. The closed symbols denote the adsorption branch of the isotherm while the open symbols indicate the desorption branch. In this presentation, the non-isothermal  $T$  variations have been transformed into their isothermal equivalent at 25 °C through Eq. (6). This allows us to directly compare the true isothermal  $P/P_0$  variations to their  $T$  variation counterpart. Notice that the physisorption isotherms are not equivalent. This means that different results would be obtained if Eq. (1) is used to quantify the pore size distributions. The reason for the discrepancy lies in the simplistic and inappropriate assumptions within the Kelvin equation. Factors like heats of the toluene adsorption and/or deviations from the bulk physical properties for the condensed toluene are probably significant. The exact reason for this failure has yet to be identified. Obviously, a more sophisticated data analysis procedure is required to fully comprehend these differences.

#### IV. SUMMARY

We present XRP as a powerful tool for characterizing the pore characteristics in low- $k$  dielectric or other smooth nanoporous film. The technique is based on gradually increasing or decreasing the partial pressure of toluene or some other adsorbate in the presence of the film and simultaneously monitoring the changes in the critical angle for total X-ray reflectance. The change in the critical angle can be converted into the volume of adsorbed condensate, and thus porosity, if the density of the condensed fluid is known or assumed to be bulk-like. Monitoring the amount of adsorbed condensate as a function of the partial pressure defines a physisorption isotherm, the basic starting point for any number of analytical interpretations. XRP directly reveals the average porosity, average film density, and average wall density of the material separating the pores. By further invoking a model of condensation (for example, the Kelvin equation for capillary condensation), it is straightforward to calculate the average pore size and pore size distribution from the physisorption isotherm. XRP has the added advantage that it directly monitors the thickness of the low- $k$  film, with Å level resolution and without knowledge of the optical constants of the film. Simultaneous thickness measurements are invaluable for determining if the adsorbed condensate swells the film. Finally, XRP has the distinct advantage of being able to resolve the density profile through the thickness dimension of the film. This is useful for perceiving porosity measurements at different depths into the films in the case of layered structures.



## V. REFERENCES

- [1] Petkov, M.P., M.H. Weber, K.G. Lynn, K.P. Rodbell, and S.A. Cohen. *Appl. Phys. Lett.* **74**, 2146 (1999).
- [2] (a) Gidley, D.W., W.E. Freize, T.L. Dull, J. Sun, A.F. Yee, C.V. Nguyen, and D.Y. Yoon. *Appl. Phys. Lett.* **76**, 1282 (2000);  
 (b) Sun, J., D.W. Gidley, T.L. Dull, W.E. Frieze, A.F. Yee, E.T. Ryan, S. Lin, and J. Wetzel. *J. Appl. Phys.* **89**, 5138 (2001);  
 (c) Dull, T.L., W.E. Frieze, D.W. Gidley, J.N. Sun, and A.F. Yee. *J. Phys. Chem. B* **105**, 4657 (2001).
- [3] (a) Baklanov, M.R., K.P. Mogilnikov, V.G. Polovkinkin, and F.N. Dultsev. *J. Vac. Sci. Technol. B* **18**, 1385 (2000);  
 (b) Baklinov, M.R., and K.P. Mogilnikov. *Optica Applicata* **30**, 491 (2000);  
 (c) Shamiryan, D.G., M.R. Baklinov, S. Vanhaelemeersch, and K. Maex. *Electrochem. Solid St.* **4**, F3 (2001);  
 (d) Murray, C., C. Flannery, I. Steiter, S.E. Schulz, M.R. Baklinov, K.P. Mogilnikov, C. Himcinschi, M. Friedrich, D.R.T. Zahn, and T. Gessner. *Microelectron. Eng.* **60**, 133 (2002);  
 (e) Baklinov, M.R., and K.P. Mogilnikov. *Microelectron. Eng.* **64**, 335 (2002).
- [4] (a) Lee, H.-J., E.K. Lin, H. Wang, W.-l. Wu, W. Chen, and E.S. Moyer. *Chem. Matter* **14**, 1845 (2002);  
 (b) Lin, E.K., H.-J. Lee, G.W. Lynn, W.-l. Wu, and M.L. O'Neill. *Appl. Phys. Lett.* **81**, 607 (2002);  
 (c) Wu, W.-l., W.E. Wallace, E.K. Lin, G.W. Lynn, C.J. Glinka, E.T. Ryan, and H.M. Ho. *J. Appl. Phys.* **87**, 1193 (2000);  
 (d) Hedden, R.C., H.-J. Lee, and B.J. Bauer. *Langmuir* **20**, 416 (2004);  
 (e) Lin, E.K., H. Lee, B.J. Bauer, H. Wang, J.T. Wetzel, W. Wu. "Structure and Property Characterization of Low-k Dielectric Porous Thin Films Determined by X-ray Reflectivity and Small-Angle Neutron Scattering." *Low Dielectric Constant Materials for IC Applications*. Eds. P.S. Ho, J. Leu, and W.W. Lee. New York: Springer Publishing (2002);  
 (f) Bauer, B.J., E.K. Lin, H.J. Lee, H. Wang, and W.-l. Wu. *J. Electron. Mater.* **30**, 304 (2001);  
 (g) Bouldin, C.E., W.E. Wallace, G.W. Lynn, S.C. Roth, and W.-l. Wu. *J. Appl. Phys.* **88**, 691 (2000).



- [5] Deitz, V.R. *Bibliography of Solid Adsorbents*. Washington, DC: National Bureau of Standards (1944).
- [6] Forrester, S.D., and C.H. Giles. *Chem & Ind.* 831 (1971).
- [7] Rouquerol, F., J. Rouquerol, and K. Sing. *Adsorption by Powders and Porous Solids: Principles, Methodology and Application*. London: Academic Press (1999).
- [8] Gregg, S.J., and K.S.W. Sing. *Adsorption, Surface Area, and Porosity*. London: Academic Press (1982).
- [9] Do, D.D. *Adsorption Analysis: Equilibria and Kinetics*. London: Imperial College Press (1998).
- [10] Zsigmondy, A. *Z. Anorg. Chem.* **71**, 356 (1911).
- [11] Thompson, W.T. (Lord Kelvin), *Phil. Mag.* **42**, 448 (1871).
- [12] Sing, K.S.W., D.H. Everett, R.A.W. Hual, L. Mocsou, R.A. Pierotti, J. Rouquerol, and T. Siemieniewska. *Pure Appl. Chem.*, **57**, 603 (1985).
- [13] Everett, D.H. *Pure Appl. Chem.* **31**, 579 (1972).
- [14] Parratt, L.G. *Phys. Rev.* **95**, 359 (1954).
- [15] Lekner, J. *Theory of Reflection*. Dordrecht: Martinus Nijhoff (1987).
- [16] Heavens, O.S. *Optical Properties of Thin Solid Films*. London: Butterworth (1955).
- [17] Russell, T.P. "X-ray and Neutron Reflectivity for the Investigation of Polymers." *Materials Science Reports* **5**, 171. North-Holland: Elsevier Science Publishers B.V. (1990).
- [18] Foster, M.D. *Critical Reviews in Analytical Chemistry* **24**, 179 (1993).
- [19] Anker, J.F., and C.J. Majkrzak. *Proc. SPIE* **1738**, 260 (1992).
- [20] (a) Chu, W.K., J.W. Mayer, and M.A. Nicolet. *Backscattering Spectrometry*. New York: Academic Press (1978);  
 (b) Tesmer, J.R., and M. Nastasi, eds. *Handbook of Modern Ion Beam Materials Analysis*. Pittsburgh: Materials Research Society Press (1995);  
 (c) Composto, R.J., R.M. Walters, and J. Genzer. *Mater. Sci. Eng. Reports* **38**, 107 (2002).
- [21] Wu, W.-l. *J. Chem. Phys.* **98**, 1687 (1993); W.-l. Wu, *J. Chem. Phys.* **101**, 4198 (1994).

- [22] Certain commercial equipment and materials are identified in this paper in order to specify adequately the experimental procedure. In no case does such identification imply recommendation by the National Institute of Standards and Technology nor does it imply the material or equipment identified is necessarily the best available for this purpose.
- [23] Gurvich, L.G. *J. Russ. Phys. Chim.* **47**, 805 (1915).
- [24] Jackson, C.L., and G.B. McKenna. *J. Chem. Phys.* **93**, 9002 (1990).
- [25] Jackson, C.L., and G.B. McKenna. *Chem. Mater.* **8**, 2128 (1996).
- [26] Dosseh, G., D. Morineau, and C. Alba-Simioneso. *J. Phys. IV* **10 (Pr7)**, 99 (2000)
- [27] Morineau, D., and C. Alba-Simioneso. *J. Chem. Phys.* **118**, 9389 (2003).
- [28] Dosseh, G., G.Y. Xia, and C. Albe-Simionesco. *J. Phys. Chem. B*, **107**, 6445 (2003).
- [29] Morishige, K., and K. Kawano. *J. Chem. Phys.* **112**, 11023 (2000).
- [30] Maddox, M., and K.E. Gubbins. *J. Chem. Phys.* **107**, 9659 (1997).
- [31] Kaneko, K., A. Watanabe, T. Iiyama, R. Radhakrishnan, and K.E. Gubbins. *J. Chem. Phys.* **103**, 7061 (1999).
- [32] Watanabe, A., and K. Kaneko. *Chem. Phys. Lett.* **305**, 71 (1999).
- [33] Sliwinska-Bartkowiak, M., R. Radhakrishnan, and K.E. Gubbins. *J. Chem. Phys.* **112**, 11048 (2000).
- [34] Mu, R., Y. Xue, D.O. Henderson, and D.O. Fraizer. *Phys. Rev. B* **53**, 6041 (1996).
- [35] Booth, H.F., and J.H. Strange. *Mol. Phys.* **93**, 263 (1998)
- [36] Strange, J.H., M. Rahman, and E.G. Smith. *Phys. Rev. Lett.* **71**, 3589 (1993).
- [37] Krim, J., J.P. Coulomb, and J. Bouzidi. *Phys. Rev. Lett.* **58**, 583 (1987).
- [38] Mu, R., and V.M. Malhotra. *Phys. Rev. B* **44**, 4296 (1991).
- [39] Aksnes, D.W., and L. Gjerdaker. *J. Mol. Struct.* **475**, 27 (1999).
- [40] Shao, Y., G. Hoang, and J.W. Zerda. *J. Non-Cryst. Solids* **182**, 309 (1995).
- [41] Gedat, E., A. Schreiber, J. Albrecht, Th. Emmmler, I. Shenderovich, G.H. Findenegg, H.-H Limbach, and G. Buntkowsky. *J. Phys. Chem. B* **106**, 1977 (2002).

- [42] Gjerdaker, L., D.W. Aksnes, G.H. Sorland, and M. Stocker. *Micropor. Mesopor. Mater.* **42**, 89, (2001).
- [43] Morineau, D., Y. Xia, and C. Alba-Simionesco. *J. Chem. Phys.* **117**, 1753 (2002).
- [44] Gallagher, M., N. Pugliano, M. Roche, J. Calvert, Y. You, R. Gore, N. Annan, M. Talley, S. Ibbitson, and A. Lamola. *MRS Spring Meeting*, San Francisco (2001).
- [45] Grill, A., and V. Patel. *Appl. Phys. Lett.* **79**, 803 (2001).
- [46] Lee, H.J., E.K. Lin, B.J. Bauer, W.L. Wu, B.K. Hwang, and W.D. Gray. *Appl. Phys. Lett.* **82**, 1084 (2003).
- [47] Kruk, M., and M. Jaroniec. *Chem. Mater.* **13**, 3169 (2001).
- [48] Kraemer, E.O. *A Treatise on Physical Chemistry*. Ed. H.S. Taylor. New York: Macmillan (1931), p. 1661.
- [49] Debye, P., H.R. Anderson, and H. Brumberger. *J. Appl. Phys.* **28**, 679 (1957).
- [50] de Boer, J.H. *The Dynamical Character of Adsorption*. London: Oxford University Press, 1968, p. 179.
- [51] Langmuir, I. *J. Am. Chem. Soc.*, **1916**, 38, 2221.; *ibid*, **1918**, 40, 1361.
- [52] Brunauer, S., P.H. Emmett, and E. Teller. *J. Am. Chem. Soc.*, **1938**, 60, 309.
- [53] Brunauer, S. *The Adsorption of Gases and Vapors*. Princeton: Princeton University Press, 1945.
- [54] Dubinin, M.M., and L.V. Radushkevich. *Proc. Acad. Sci. USSR*, **1947**, 55, 331.
- [55] Stoeckli, H.F. *J. Colloid Interface Sci.*, **1977**, 59, 184.
- [56] Barrett, E.P., L.G. Joyner, and P.H. Halenda. *J. Am. Chem. Soc.*, **1951**, 73, 373.
- [57] Broekhoff, J.C.P., and J. de Boer. *Catalysis*, **1967**, 9, 8.
- [58] Neimark, A., P.I. Ravikovitch, and A. Vishnyakov. *Phys. Rev. E* **2000**, 62, R1493.
- [59] Neimark, A.V., F. Schuth., and K.K. Unger. *Langmuir* **1995**, 11, 4765
- [60] Ravikovitch, P.I., A. Vishnyakov, and A. Neimark. *Phys. Rev. E* **2001**, 64, 011602.



